Electronic Supplementary Information (ESI†) for

Cu(II) flavonoids as potential photochemotherapeutic agents

Namisha Das,[a] Bidisha Bora,[a] Aarti Upadhyay,[b] Dhananjay Das,[a] Arpan Bera,*[,b] and Tridib K. Goswami *[,a]

[a] *Department of Chemistry, Gauhati University, Guwahati 781014, Assam, India*

[b] *Department of Inorganic and Physical Chemistry, Indian Institute of Science, Bangalore 560012, India*

Table of Contents

Table S1. Mass spectral data for the complexes **1-6** in acetonitrile.

Table S2. Cathodic and anodic current densities and their ratio for the Cu(II)/Cu(I) redox couple for the complexes **1-6** in DMF.

Table S3. EPR parameters of complex **2** in solid and solution phases.

Table S4. Selected bond distances (Å) and bond angles (º) of $[Cu(L_1)(phen)](ClO_4)$ (**2**), where L_1 is monoanionic form of 4-fluoro-3-hydroxyflavone.

Table S5. Selected crystallographic data for the ligand 3-hydroxyflavone.

Table S6. Selected crystallographic data for the ligand 2,6-difluoro-3-hydroxyflavone.

Table S7. DNA and human serum albumin (HSA) binding constants for the complexes **1-6**.

Table S8. Rate constants (*k*) of singlet oxygen generation obtained from first order plot for the complexes **1-6**.

Scheme S1. Synthetic schemes of the complexes **1-6**.

Fig. S1-S3 ESI Mass spectra of the ligands 3-hydroxy flavone, 4-fluoro-3-hydroxy flavone and 2,6-difluoro-3-hydroxy flavone in methanol showing the $[M+H]^+$ peaks.

Fig. S4-S6 ^1H NMR spectra of the ligands 3-hydroxy flavone, 4-fluoro-3-hydroxy flavone and 2,6-difluoro-3-hydroxy flavone in $CDCl_3$.

Fig. S7-S12 IR spectra of the complexes **1-6** in solid KBr matrix.

Fig. S13-S18 ESI Mass spectra of the complexes **1-6** in acetonitrile showing the $[M-(ClO_4^-)]^+$ peaks.

Fig. S19 UV-visible spectra of **1-6** (25 μM) in DMSO-DMEM (1:9 v/v) showing the ligand-centered bands.

Fig. S20 Cyclic voltammetric responses of complex **1-3** in DMF at a scan rate of 50 mVs^{-1} using TBAP (0.1 M) as the supporting electrolyte.

Fig. S21 Cyclic voltammetric responses of complex **1-3** in DMF at a scan rate of 50 mVs^{-1} using TBAP (0.1 M) as the supporting electrolyte.

Fig. S22 Cyclic voltammetric responses of the complexes **1** (a & b), **2** (c & d) and **3** (e & f) showing the anodic and cathodic responses corresponding to the flavonoids and phenanthroline bases present in the complexes in DMF at a scan rate of 50 mVs^{-1} using TBAP (0.1 M) as the supporting electrolyte.

Fig. S23 Cyclic voltammetric responses of the complexes **4** (a & b), **5** (c & d) and **6** (e & f) showing the anodic and cathodic responses corresponding to the flavonoids and phenanthroline

bases present in the complexes in DMF at a scan rate of 50 mVs^{-1} using TBAP (0.1 M) as the supporting electrolyte.

Fig. S24 UV-visible spectra of the complexes **1** (a & b), **2** (c & d) and **3** (e & f) recorded in DMSO-Tris-HCl buffer (1:9, pH 7.2) for a period of 24 h.

Fig. S25 UV-visible spectra of the complexes **4** (a & b), **5** (c & d) and **6** (e & f) recorded in DMSO-Tris-HCl buffer (1:9, pH 7.2) for a period of 24 h.

Fig. S26 UV-visible spectra of the complexes **1** (a & b), **2** (c & d) and **3** (e & f) recorded in DMSO-DMEM (1:9 v/v) showing their photostability on exposure to visible light for a period of 60 min.

Fig. S27 UV-visible spectra of the complexes **4** (a & b), **5** (c & d) and **6** (e & f) recorded in DMSO-DMEM (1:9 v/v) showing their photostability on exposure to visible light for a period of 60 min.

Fig. S28 UV-visible spectral changes of the complexes **1** (a & b), **2** (c & d) and **3** (e & f) recorded in DMSO-DMEM (1:9 v/v) for a period of 24 h upon treatment with GSH (3 mM).

Fig. S29 UV-visible spectral changes of the complexes **4** (a & b), **5** (c & d) and **6** (e & f) recorded in DMSO-DMEM (1:9 v/v) for a period of 24 h upon treatment with GSH (3 mM).

Fig. S30 EPR spectra of complex **2** in solid (a) and solution (DMSO) (b) phases at 77K.

Fig. S31 Unit cell packing diagram for the complex $[Cu(L_1)(phen)](ClO_4)$ (**2**), where L_1 is monoanion of 4-fluoro-3-hydroxy flavone.

Fig. S32 Unit cell packing diagram of ligand 3-hydroxy flavone.

Fig. S33 Unit cell packing diagram of ligand 2,6-difluoro-3-hydroxy flavone.

Fig. S34 ORTEP view of the ligand 3-hydroxy flavone showing 30% probability thermal ellipsoids.

Fig. S35 ORTEP view of the ligand 2,6-difluoro-3-hydroxy flavone showing 30% probability thermal ellipsoids.

Fig. S36 Absorption spectral traces of the complexes **1-3** (a-c) in 5 mM Tris-HCl buffer (pH 7.2) on increasing the quantity of calf thymus DNA. The inset shows the least square fits of $\Delta\varepsilon_{af}/\Delta\varepsilon_{bf}$ *vs.* [DNA] for the complexes using McGhee-von Hippel (MvH) method.

Fig. S37 Absorption spectral traces of the complexes **4-6** (a-c) in 5 mM Tris-HCl buffer (pH 7.2) on increasing the quantity of calf thymus DNA. The inset shows the least square fits of $\Delta\varepsilon_{af}/\Delta\varepsilon_{bf}$ *vs.* [DNA] for the complexes using McGhee-von Hippel (MvH) method.

Fig. S38 Emission spectral traces of HSA (2 μM) in the presence of complexes **1-3** (a-c). The inset shows the plot of (I_0/I) *vs.* [complex].

Fig. S39 Emission spectral traces of HSA (2 μM) in the presence of complexes **4-6** (a-c). The inset shows the plot of (I_0/I) *vs.* [complex].

Fig. S40 Fluorescence spectra of HTA solution resulting from the reaction of TA (2 mM) with •OH radical generated by the complexes (a) **1**, (b) **2** and (c) **3** (25 μM) on exposure to visible light for different time interval.

Fig. S41 Fluorescence spectra of HTA solution resulting from the reaction of TA (2 mM) with •OH radical generated by the complexes (a) **4**, (b) **5** and (c) **6** (25 μM) on exposure to visible light for different time interval.

Fig. S42 A comparison of the increase in concentration of HTA from the reaction of TA (2 mM) with •OH radical generated by the complexes **1**-**6** (25 μM) on exposure to visible light for different time interval.

Fig. S43 Absorption spectral traces of 1,3-diphenylisobenzofuran (DPBF) (1 mM) in presence of complexes (a) **1**, (c) **2** and (e) **3** (25 μM) on visible light irradiation for different time interval indicating generation of $^1O_2$. The panels (b) **1**, (d) **2** and (f) **3** show the first-order plot of absorbance of DPBF versus irradiation time for the complexes.

Fig. S44 Absorption spectral traces of 1,3-diphenylisobenzofuran (DPBF) (1 mM) in presence of complexes (a) **4**, (c) **5** and (e) **6** (25 μM) on visible light irradiation for different time interval indicating generation of $^1O_2$. The panels (b) **4**, (d) **5** and (f) **6** show the first-order plot of absorbance of DPBF versus irradiation time for the complexes.

Fig. S45 Absorption spectral traces of 1,3-diphenylisobenzofuran (DPBF) (1 mM) in presence of complexes (a) **1**, (b) **2**, (c) **3**, (d) **4**, (e) **5** and (e) **6** (25 μM) in dark at different time interval indicating that there is no significant generation of $^1O_2$.

Fig. S46-S50 Cell viability plots showing the cytotoxic effect of complex **1-5** in (a) MCF-7 and (b) A549 cells in dark (black) and in the presence of visible light (red, 400-700 nm, 10 J cm^{-2}, 1 h).

Fig. S51 Cell viability plots showing the cytotoxic effect of the complex **1**-**6** in HPL1D cells in dark (black) and in the presence of visible light (green, 400-700 nm, 10 J cm^{-2}, 1 h).

Table S1. Mass spectral data for the complexes **1**-**6** in acetonitrile.

Complex	Molecular formula	Calculated m/z $[M-(ClO_4)]^+$	Experimental m/z $[M-(ClO_4)]^+$
1	$[Cu(HF_1)(phen)]ClO_4$	480.0535	480.1063
2	$[Cu(HF_2)(phen)]ClO_4$	498.0441	498.0460
3	$[Cu(HF_3)(phen)]ClO_4$	516.0347	516.1758
4	$[Cu(HF_1)(aip)]ClO_4$	696.1223	696.1470
5	$[Cu(HF_2)(aip)]ClO_4$	714.1128	714.1206
6	$[Cu(HF_3)(aip)]ClO_4$	732.1034	732.1679

Table S2. Cathodic and anodic current densities and their ratio for the Cu(II)/Cu(I) redox couple for the complexes **1**-**6** in DMF.

Complex	ic_p	ic_a	ic_p/ ic_a
1	4.806	4.400	1.09
2	4.381	4.050	1.08
3	4.071	3.862	1.05
4	5.501	5.741	0.95
5	3.900	4.394	0.90
6	4.008	3.900	1.02

Table S3. EPR parameters of complex **2** in solid and solution phases.

Sample type	g_x	g_y	g_z	R[a]	ground state	geometry
Powder	2.21	2.21	2.05	∞	d_z^2	Square pyramid
Solution[b]	2.37	2.093	2.001	0.332 (<1)	$C_1\|d_z^2\rangle + C_2\|d_{x^2-y^2}\rangle$	Intermediate Square pyramid-trigonal bipyramid

[a] $R = g_y - g_z/g_x - g_y$

[b] in DMSO

Table S4. Selected bond distances (Å) and bond angles (º) of $[Cu(L_1)(phen)](ClO_4)$ (**2**), where L_1 is monoanionic form of 4-fluoro-3-hydroxyflavone.

Cu1-O1	1.920(2)	O2-Cu1-N2	172.92(11)
Cu1-O2	1.936(2)	O1-Cu1-N1	179.43(11)
Cu1-N1	1.965(3)	O2-Cu1-N1	94.56(11)
Cu1-N2	1.979(3)	N1-Cu1-N2	83.94(12)
Cu2-O4	1.916(2)	O4-Cu2-O5	85.79(10)
Cu2-O5	1.940(3)	O4-Cu2-N4	178.01(11)
Cu2-N3	1.982(3)	O5-Cu2-N4	95.86(11)
Cu2-N4	1.977(3)	O4-Cu2-N3	94.78(11)
O1-Cu1-O2	86.01(10)	O5-Cu2-N3	172.74(11)
O1-Cu1-N2	95.49(11)	N4-Cu2-N3	83.73(12)

Table S5. Selected crystallographic data for the ligand 3-hydroxyflavone.

Empirical formula	$C_{15}H_{10}O_3$
Fw, g M^{-1}	238.23
Crystal system	orthorhombic
Space group	$P2_12_12_1$
a, Å	5.4597(5)
b, Å	11.4059(12)
c, Å	18.1880(16)
α, °	90
β, °	90
γ,°	90
V, Å^3	1132.62(19)
Z	4
T, K	296(2)
ρ_{calcd}, g cm^{-3}	1.397
λ, Å (Mo-Kα)	0.71073
μ, cm^{-1}	0.098
Data / restraints / parameters	2871 / 0 / 168
F(000)	496
Goodness-of-fit	1.060
R (F_o)[a], I>2σ(I) [Rw (F_o)[b]]	0.0407 [0.0872]
R (all data) [Rw (all data)]	0.0514 [0.0923]
Largest diff. peak and hole (e Å^{-3})	0.168, -0.184

[a] $R = \Sigma||F_o|-|F_c||/\Sigma|F_o|$, [b] $Rw = \{\Sigma[w(F_o^2-F_c^2)^2]/\Sigma[w(F_o)^2]\}^{½}$; $w = [\sigma^2(F_o)^2 + (AP)^2 + BP]^{-1}$, where $P = (F_o^2 + 2F_c^2)/3$, A = 0.0432; B = 0.0366.

Table S6. Selected crystallographic data for the ligand 2,6-difluoro-3-hydroxyflavone.

Empirical formula	$C_{15}H_8F_2O_3$
Fw, g M^{-1}	274.21
Crystal system	monoclinic
Space group	*P*21/c
a, Å	10.7113(18)
b, Å	15.507(2)
c, Å	7.1679(10)
α, °	90
β, °	91.00
γ,°	90
V, $Å^3$	1190.4(3)
Z	4
T, K	296(2)
ρ_{calcd}, g cm^{-3}	1.530
λ, Å (Mo-Kα)	0.71073
μ, cm^{-1}	0.127
Data / restraints / parameters	3028 / 0 / 186
F(000)	560
Goodness-of-fit	1.072
R (F_o)[a], I>2σ(I) [*Rw* (F_o)[b]]	0.0643 [0.0803]
R (all data) [*Rw* (all data)]	0.1613 [0.1771]
Largest diff. peak and hole (e $Å^{-3}$)	0.440, -0.463

[a] $R = \Sigma||F_o|-|F_c||/\Sigma|F_o|$, [b] $Rw = \{\Sigma[w(F_o^2-F_c^2)^2]/\Sigma[w(F_o)^2]\}^{½}$; $w = [\sigma^2(F_o)^2 + (AP)^2 + BP]^{-1}$, where $P = (F_o^2 + 2F_c^2)/3$, A = 0.1108; B = 0.

Table S7. DNA and human serum albumin (HSA) binding constants for the complexes **1-6**.

Complex	Binding constant (M^{-1})	
	HSA	*ct*-DNA
1	6.28 (±0.13) × 10^4	3.96 (±0.16) × 10^5
2	9.86 (±0.10) × 10^4	5.47 (±0.02) × 10^5
3	1.03 (±0.01) × 10^5	5.85 (±0.25) × 10^5
4	1.05 (±0.01) × 10^5	6.51 (±0.02) × 10^5
5	1.26 (±0.02) × 10^5	7.76 (±0.30) × 10^5
6	1.70 (±0.02) × 10^5	9.91 (±0.23) × 10^5

Table S8. Rate constants (k) of singlet oxygen generation obtained from first order plot for the complexes **1-6**.

Complex	Rate constant (k)/ min
1	$1.76\ (\pm 0.04) \times 10^{-2}$
2	$2.28\ (\pm 0.07) \times 10^{-2}$
3	$3.04\ (\pm 0.08) \times 10^{-2}$
4	$3.10\ (\pm 0.05) \times 10^{-2}$
5	$3.16\ (\pm 0.07) \times 10^{-2}$
6	$4.67\ (\pm 0.11) \times 10^{-2}$

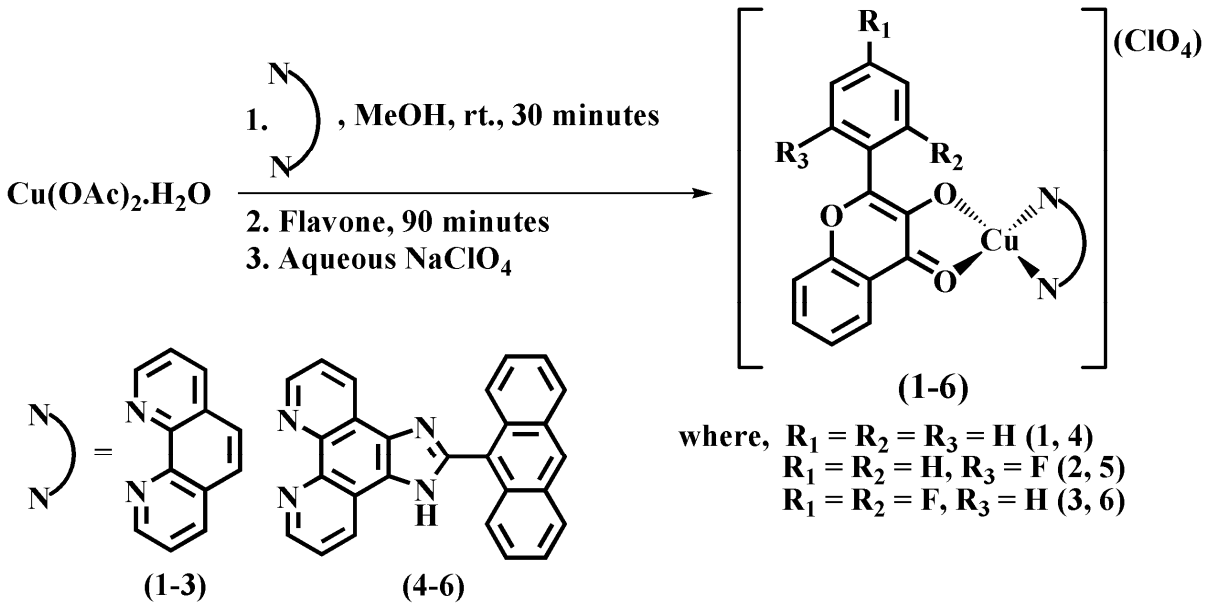

Scheme S1 Synthetic schemes of the complexes **1-6.**

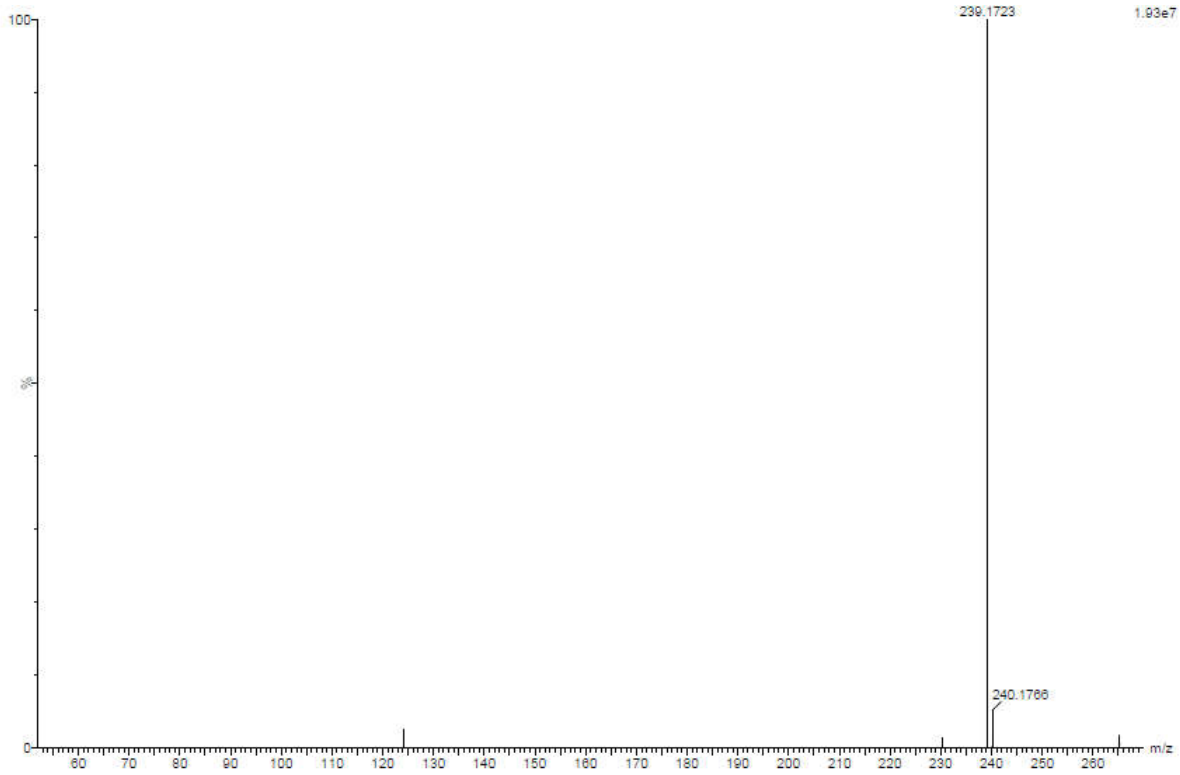

Fig. S1 ESI Mass spectrum of the ligand 3-hydroxy flavone in methanol showing the $[M+H]^+$ peak at m/z = 239.1723.

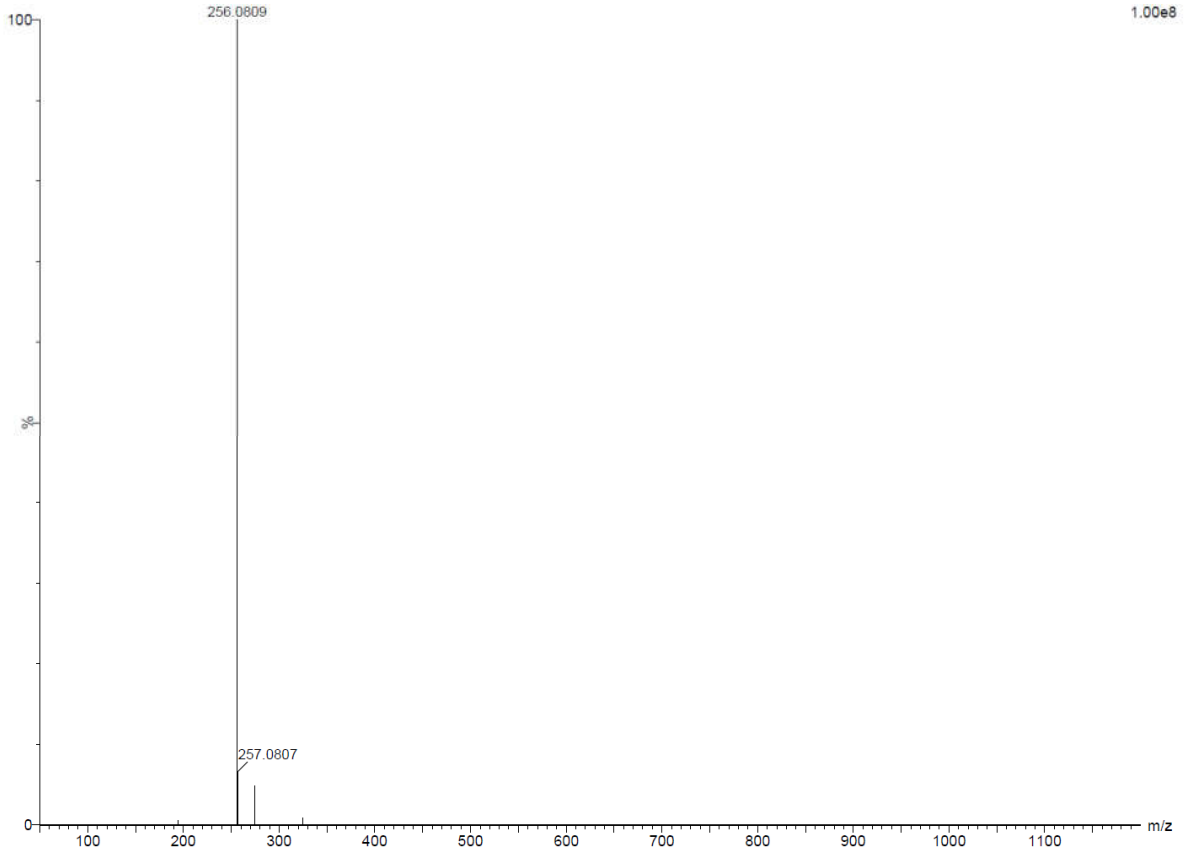

Fig. S2 ESI Mass spectrum of the ligand 4-fluoro-3-hydroxy flavone in methanol showing the $[M+H]^+$ peak at m/z = 256.0809.

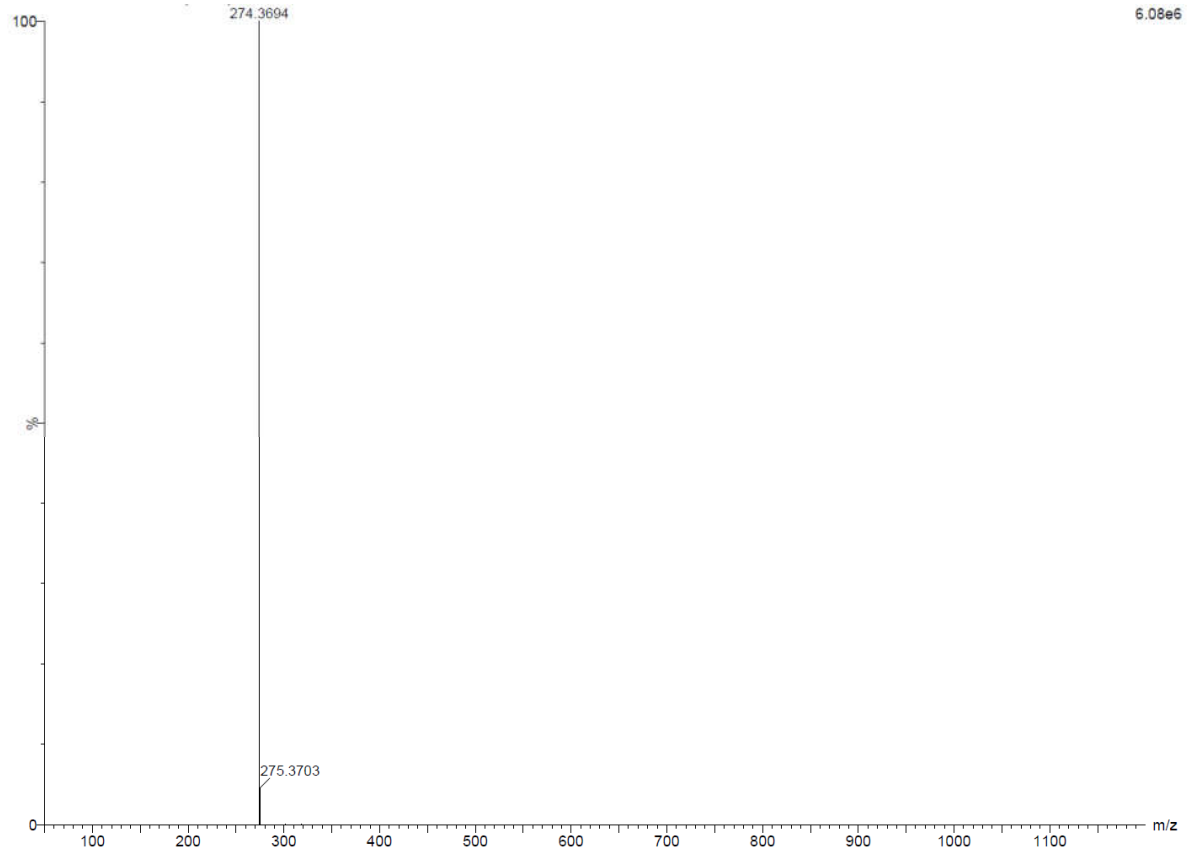

Fig. S3 ESI Mass spectrum of the ligand 2,6-difluoro-3-hydroxy flavone in methanol showing the $[M+H]^+$ peak at m/z = 274.3694.

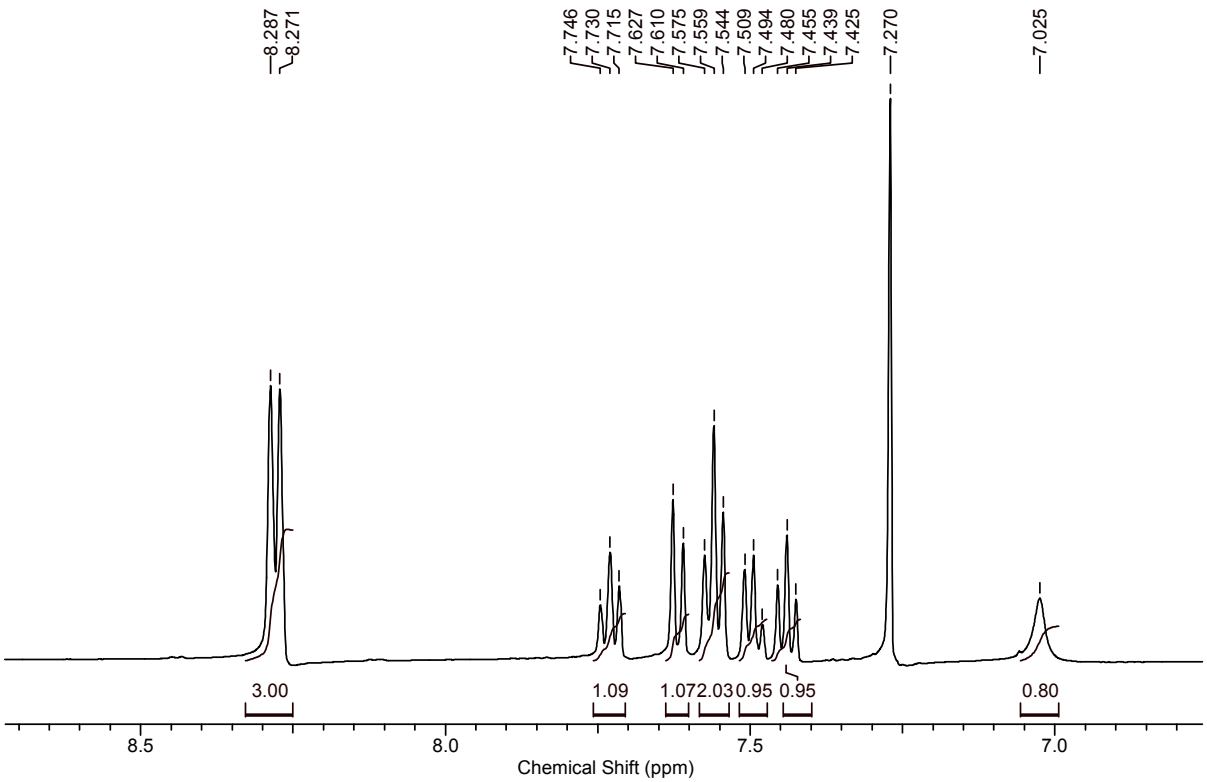

Fig. S4 ^{1}H NMR spectrum of the ligand 3-hydroxy flavone in $CDCl_3$.

^{1}H NMR (500 MHz, $CDCl_3$): 8.27(d, *J*=8, 3H), 7.73(t, *J*=8, 1H), 7.61(d, *J*=8.5, 1H), 7.55(t, *J*=8, 2H), 7.50-7.48(m, 1H), 7.43(t, *J*=8, 1H), 7.02(s, 1H).

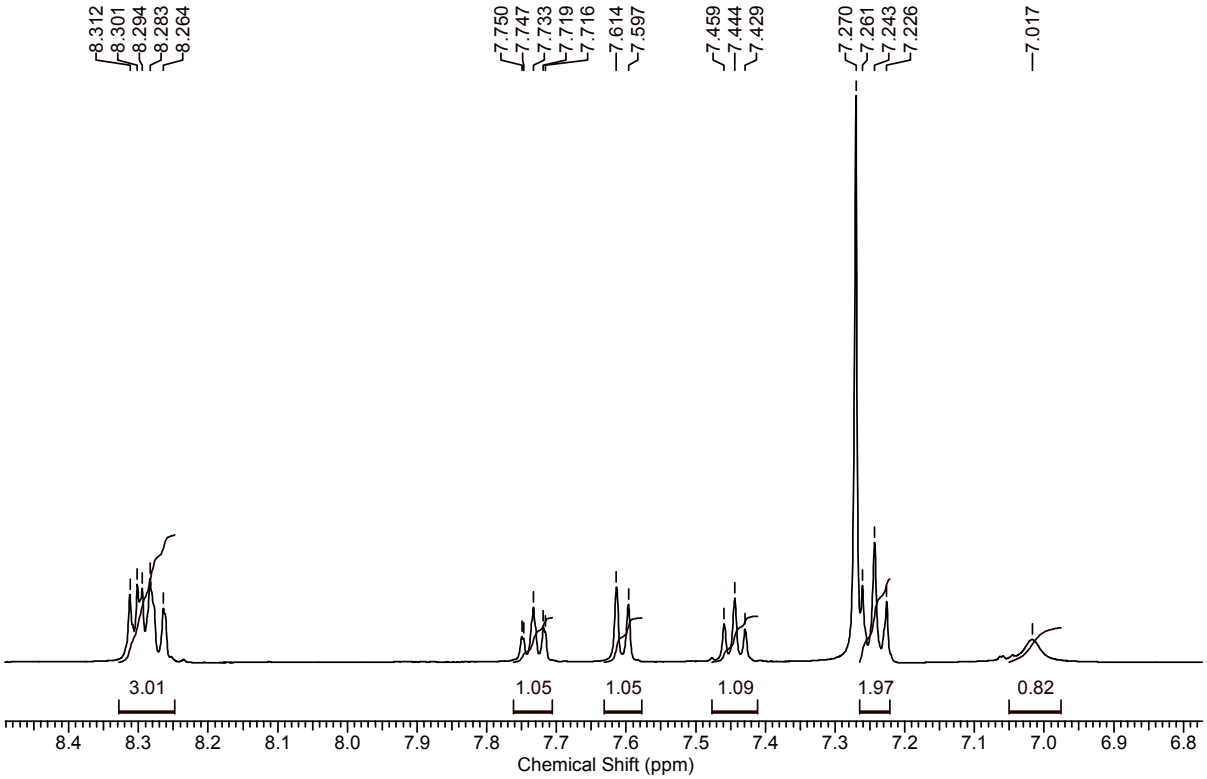

Fig. S5 ^{1}H NMR spectrum of the ligand 4-fluoro-3-hydroxy flavone in $CDCl_3$.

^{1}H NMR (500 MHz, $CDCl_3$): 8.31-8.26(m, 3H), 7.75-771(m, 1H), 7.60(d, *J*=8.5, 1H), 7.44(t, *J*=7.5, 1H), 7.26-7.11(m, 2H), 7.01(s, 1H).

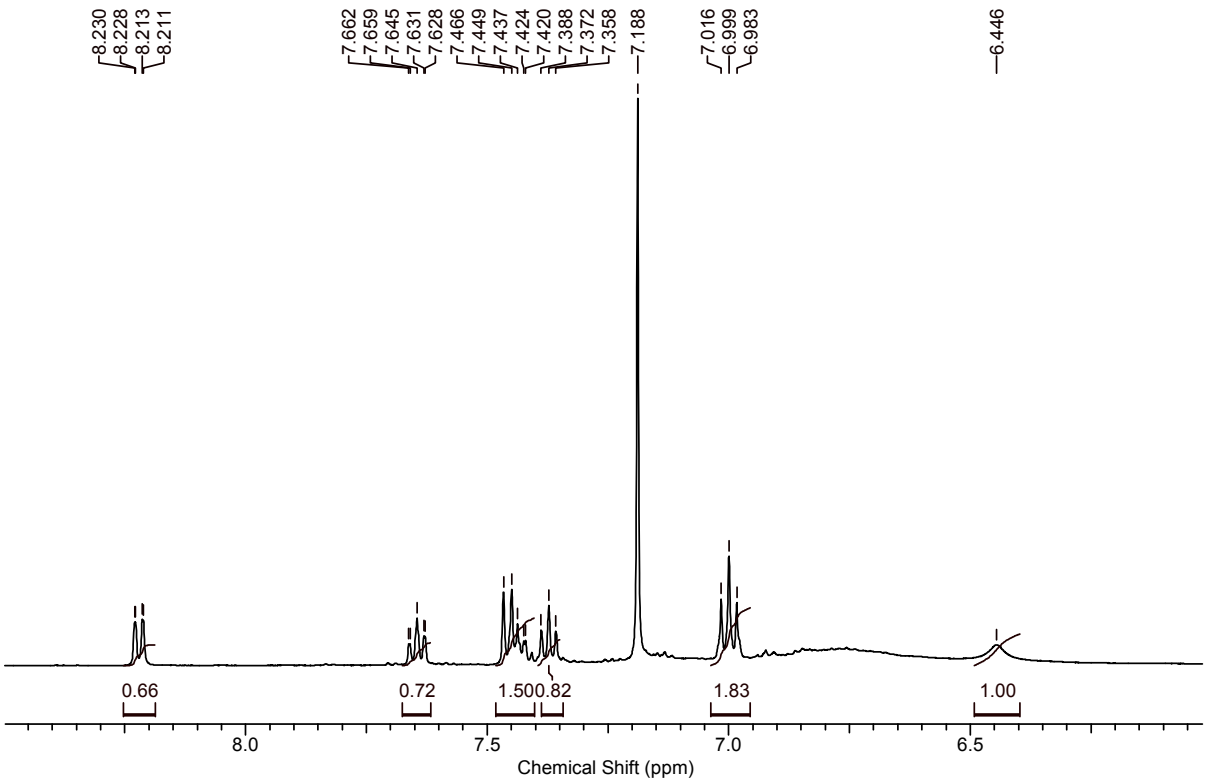

Fig. S6 ^{1}H NMR spectrum of the ligand 2,6-difluoro-3-hydroxy flavone in $CDCl_3$.

^{1}H NMR (500 MHz, $CDCl_3$): 8.23-8.21(m, 1H), 7.66-7.62(m, 1H), 7.46-7.40(m, 2H), 7.37(t, *J*=8, 1H), 6.99(t, *J*=8.5, 2H), 6.44(s, 1H).

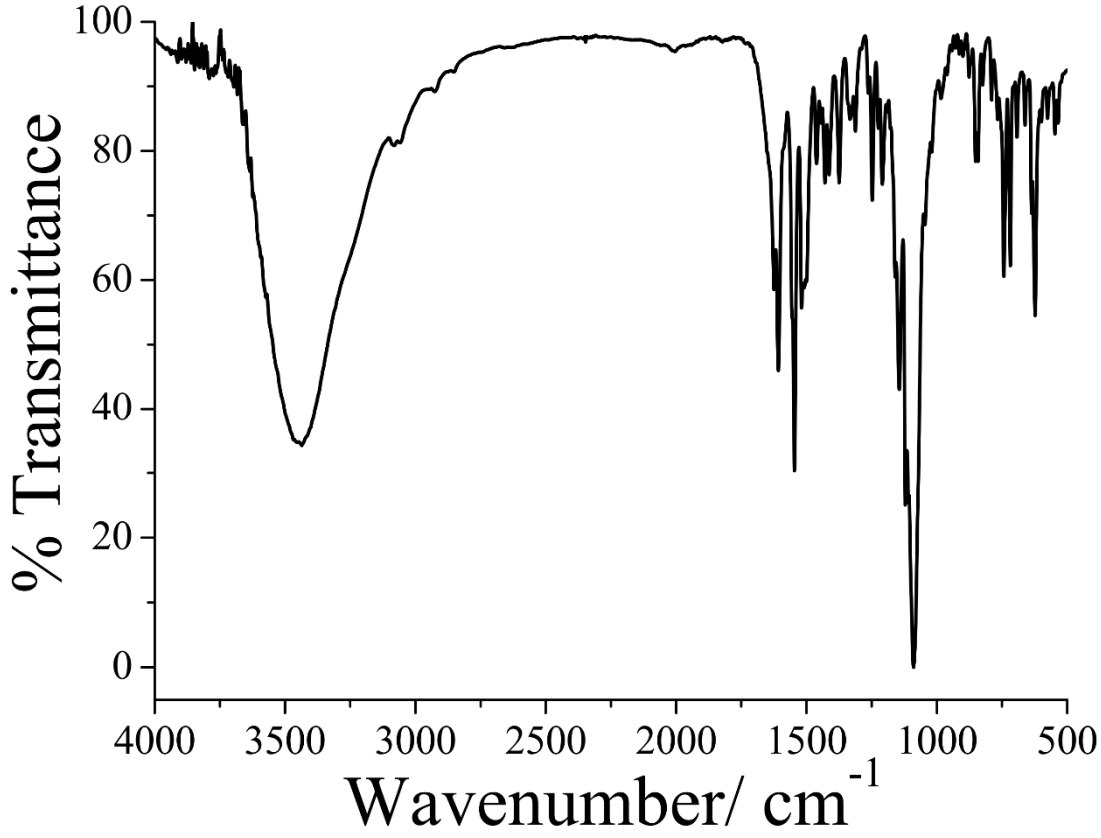

Fig. S7 IR spectrum of complex **1** in solid KBr matrix.

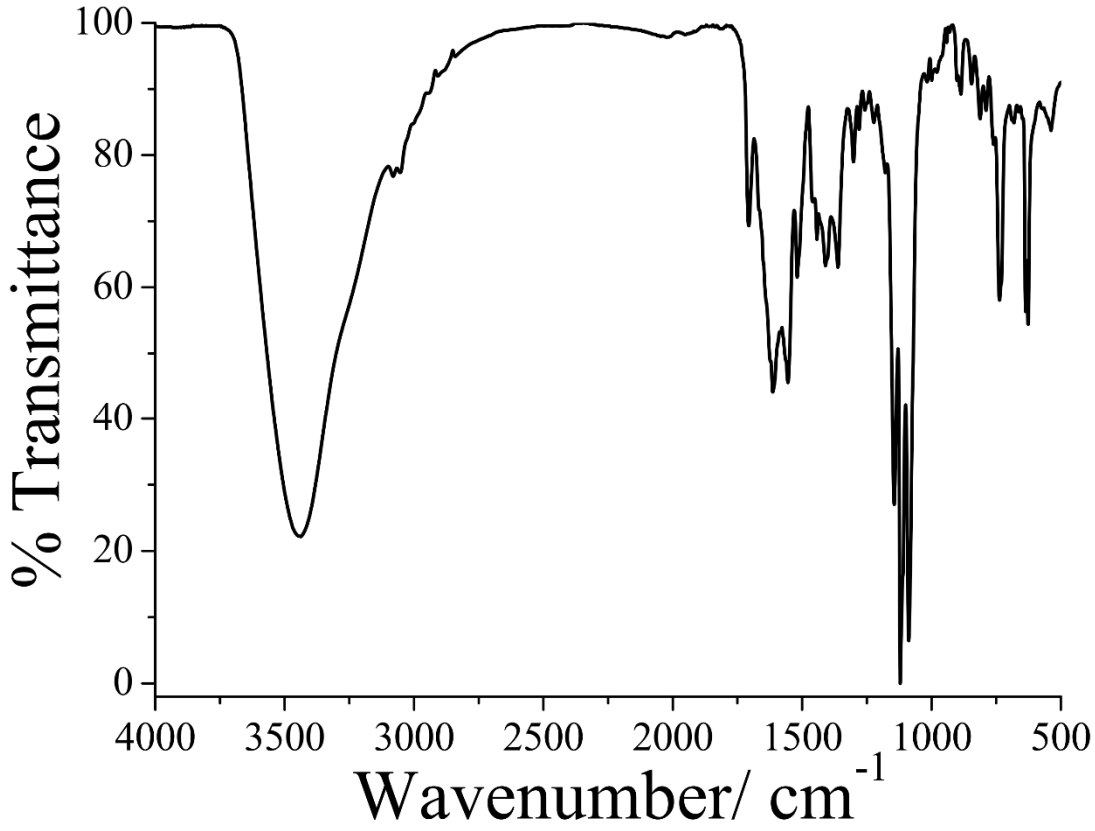

Fig. S8 IR spectrum of complex **2** in solid KBr matrix.

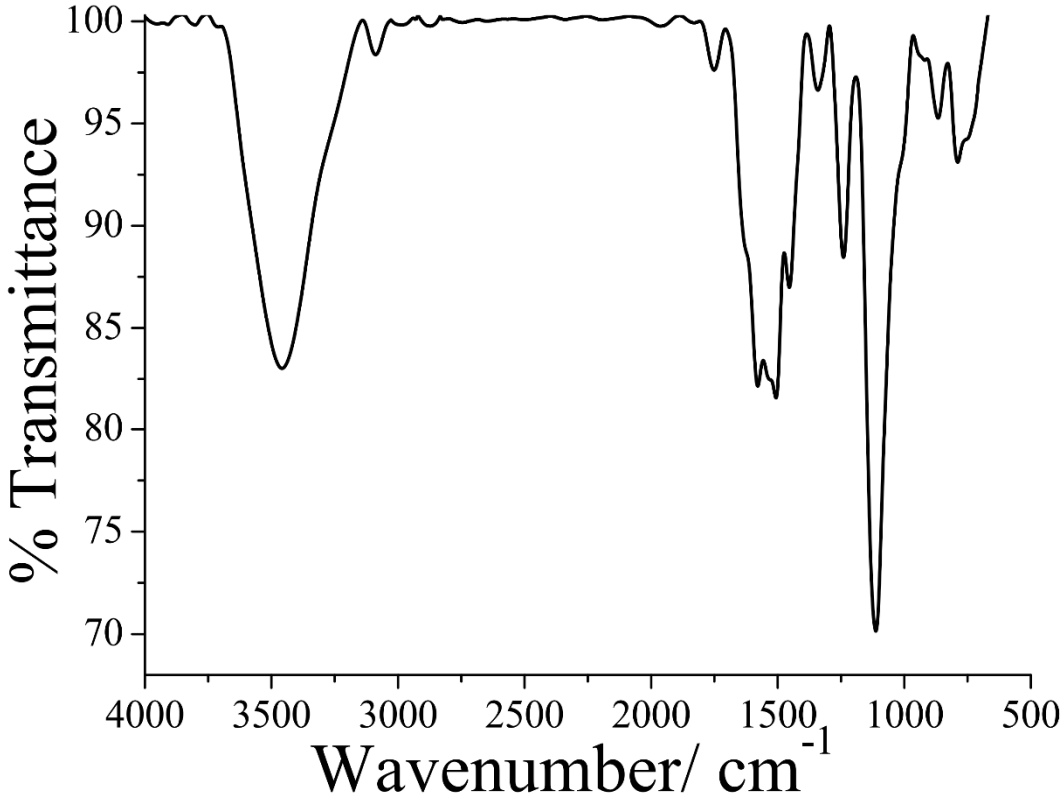

Fig. S9 IR spectrum of complex **3** in solid KBr matrix.

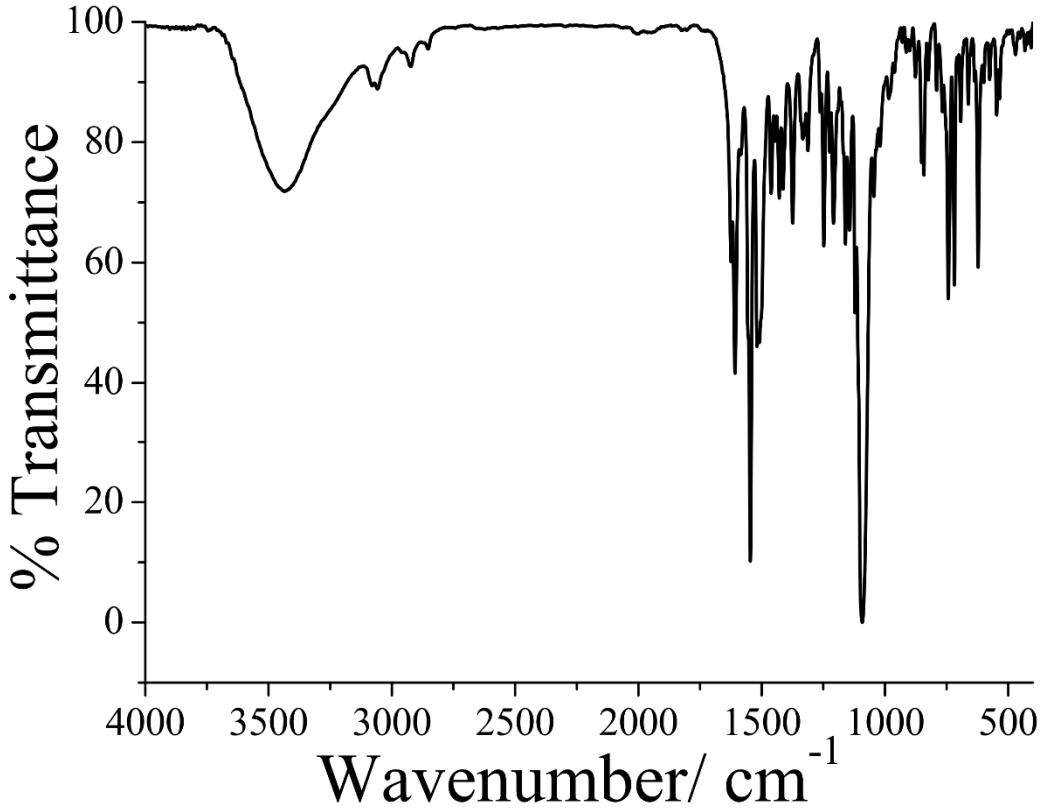

Fig. S10 IR spectrum of complex **4** in solid KBr matrix.

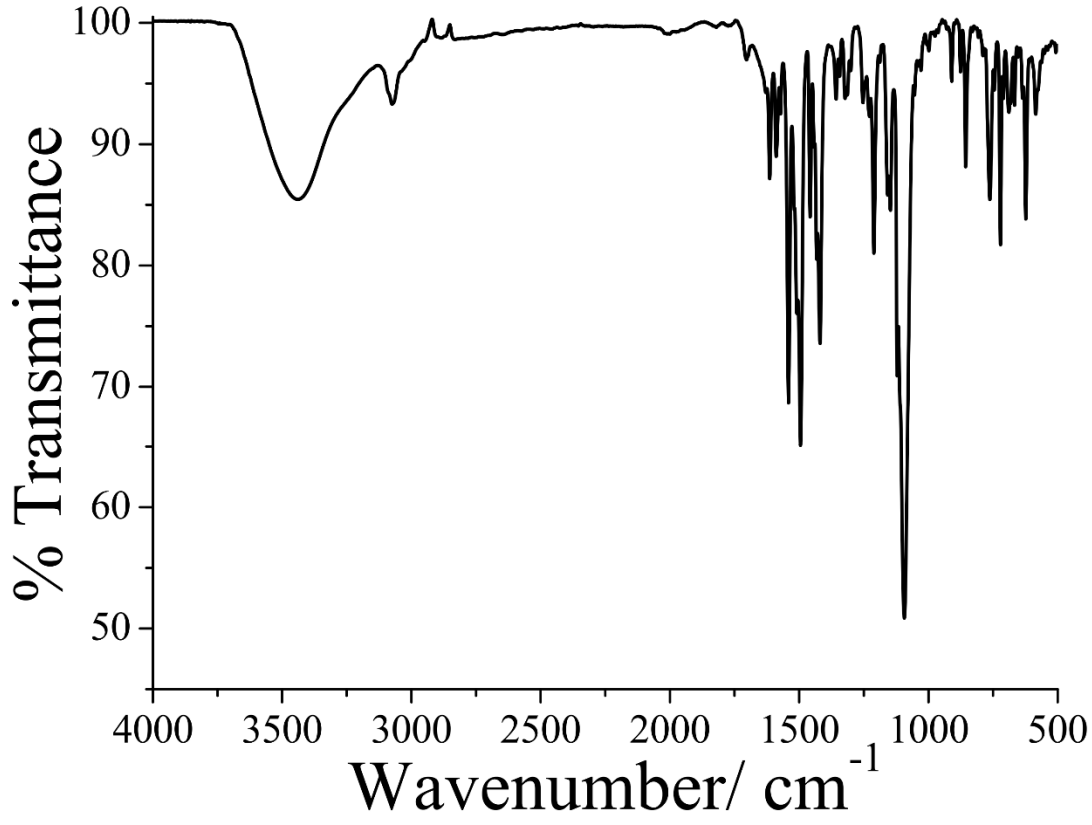

Fig. S11 IR spectrum of complex **5** in solid KBr matrix.

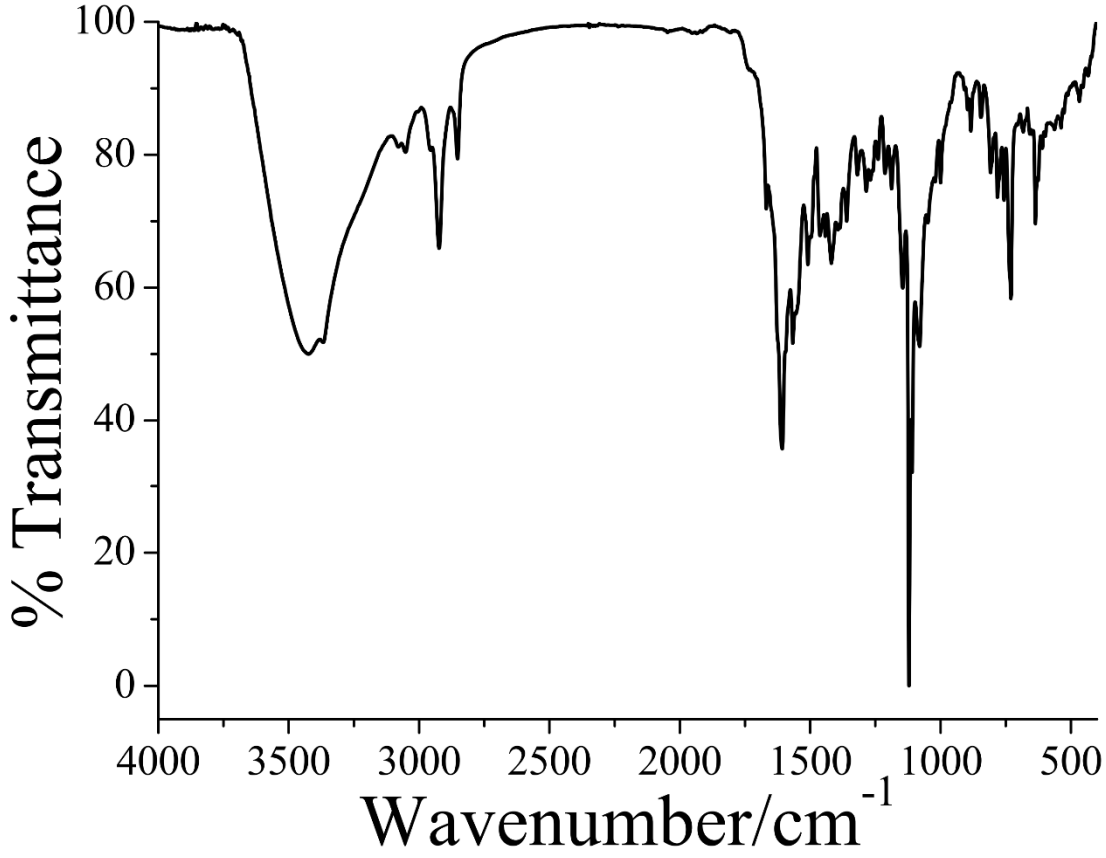

Fig. S12 IR spectrum of complex **6** in solid KBr matrix.

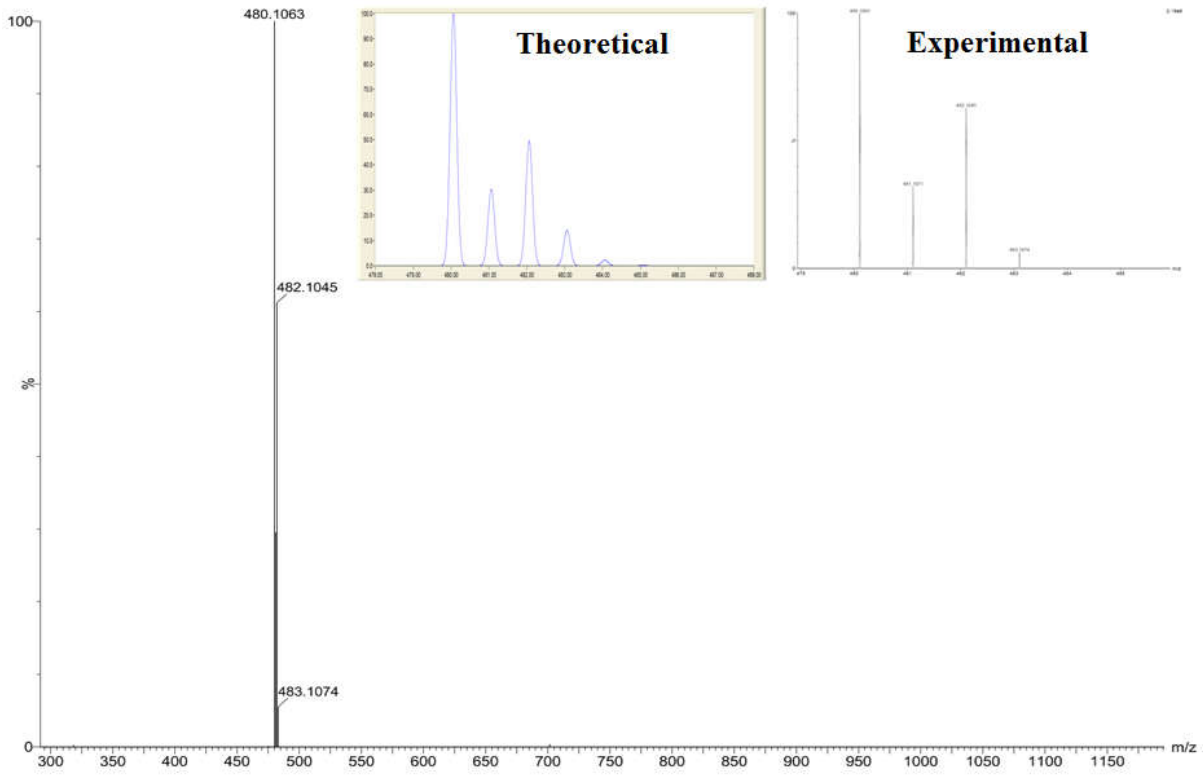

Fig. S13 ESI Mass spectrum of complex **1** in acetonitrile showing the $[M-(ClO_4^-)]^+$ peak at m/z = 480.1063. The inset shows the theoretical and experimental isotopic distributions for the complex.

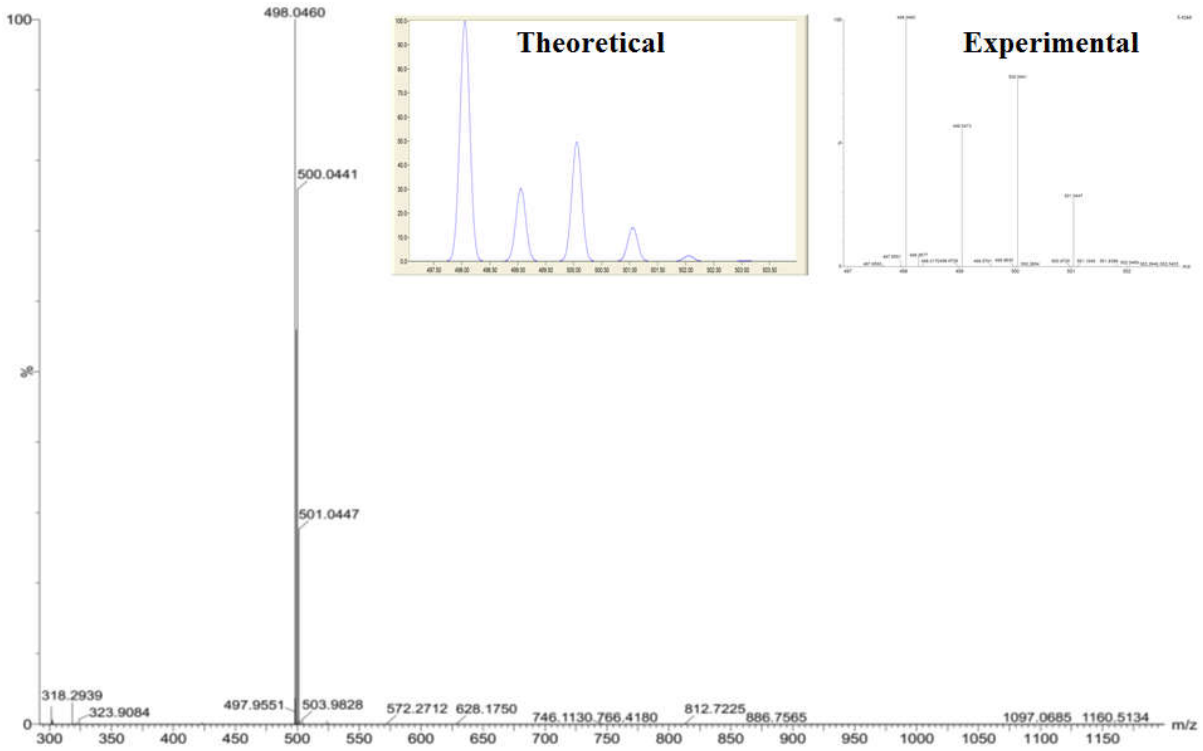

Fig. S14 ESI Mass spectrum of complex **2** in acetonitrile showing the $[M-(ClO_4^-)]^+$ peak at m/z = 498.0460. The inset shows the theoretical and experimental isotopic distributions for the complex.

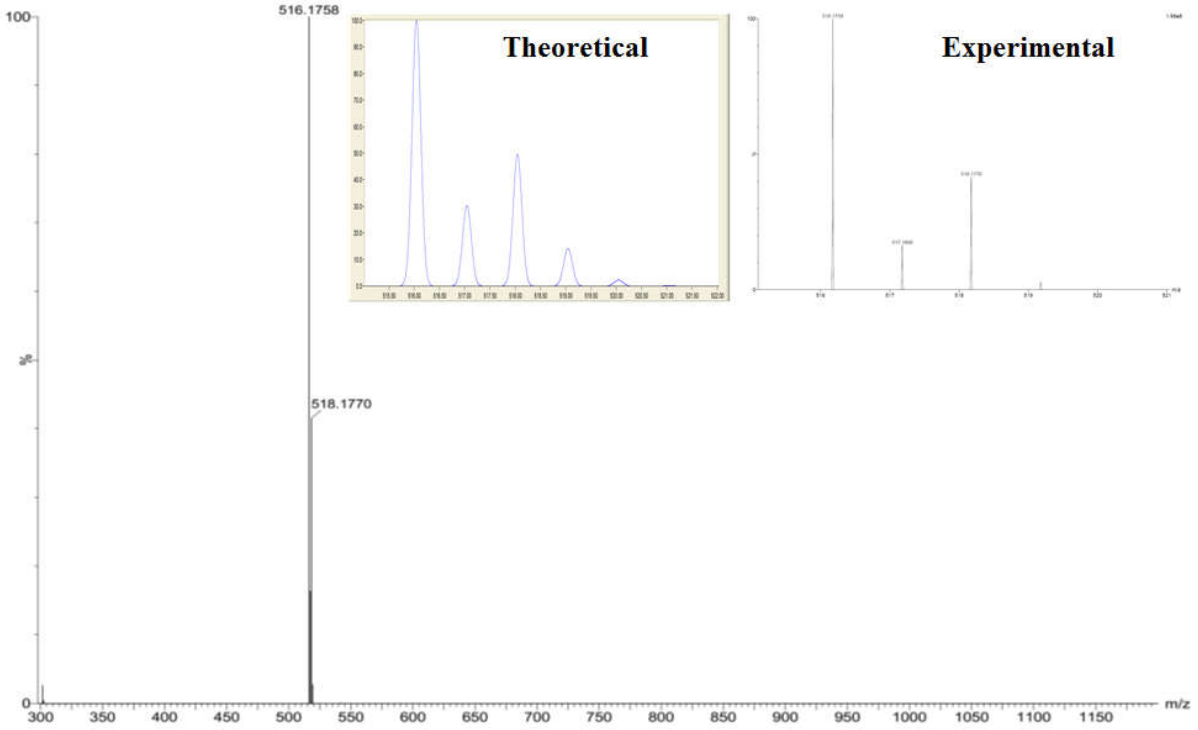

Fig. S15 ESI Mass spectrum of complex **3** in acetonitrile showing the $[M-(ClO_4^-)]^+$ peak at m/z = 516.1758. The inset shows the theoretical and experimental isotopic distributions for the complex.

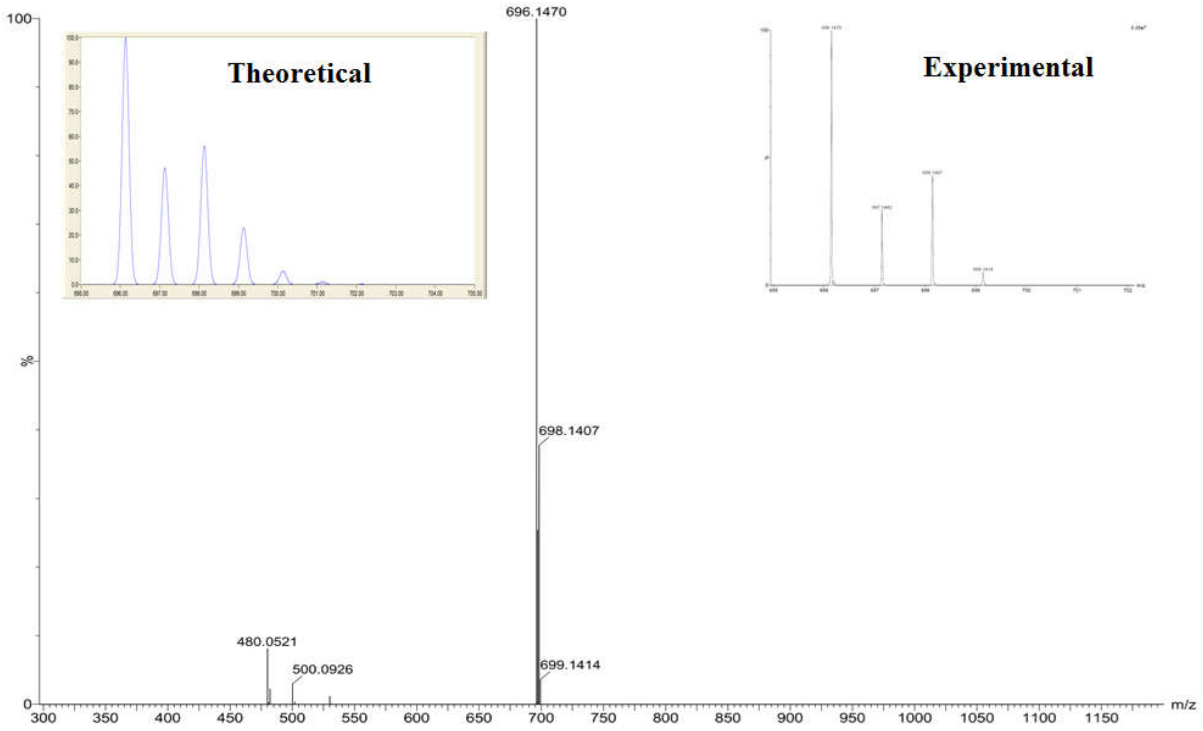

Fig. S16 ESI Mass spectrum of complex **4** in acetonitrile showing the $[M-(ClO_4^-)]^+$ peak at m/z = 696.1470. The inset shows the theoretical and experimental isotopic distributions for the complex.

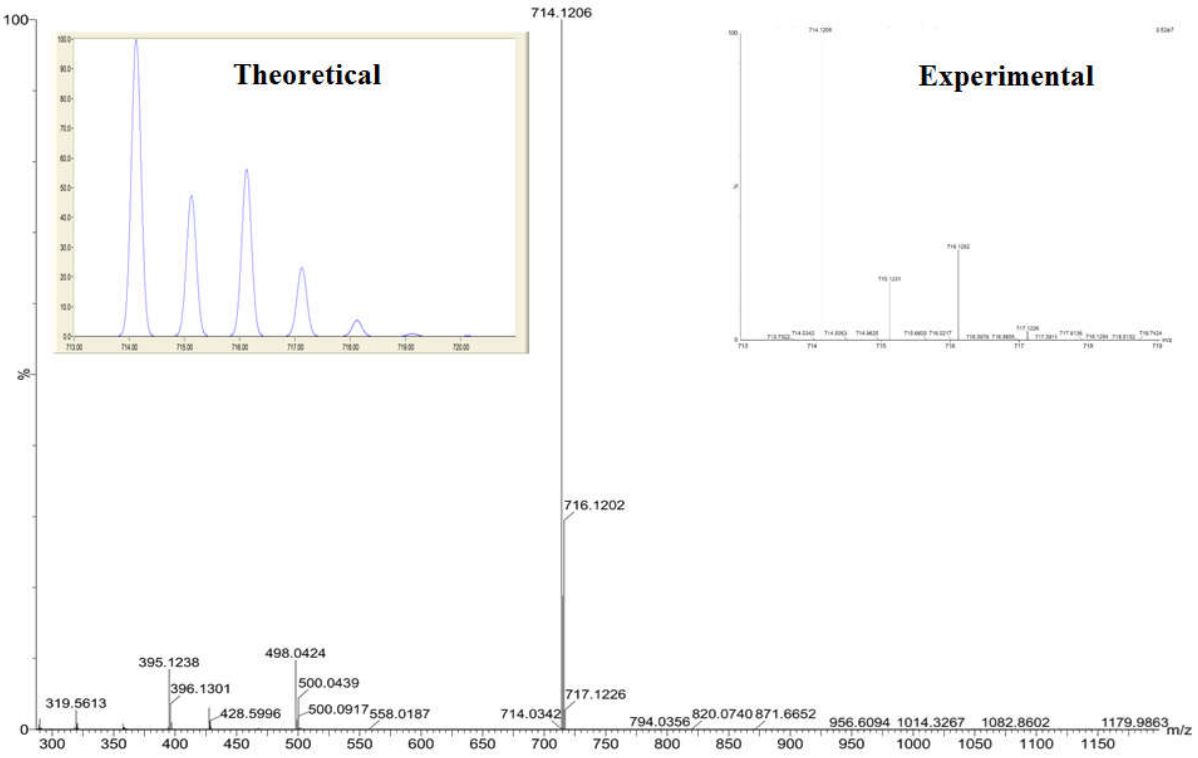

Fig. S17 ESI Mass spectrum of complex **5** in acetonitrile showing the $[M-(ClO_4^-)]^+$ peak at m/z = 714.1206. The inset shows the theoretical and experimental isotopic distributions for the complex.

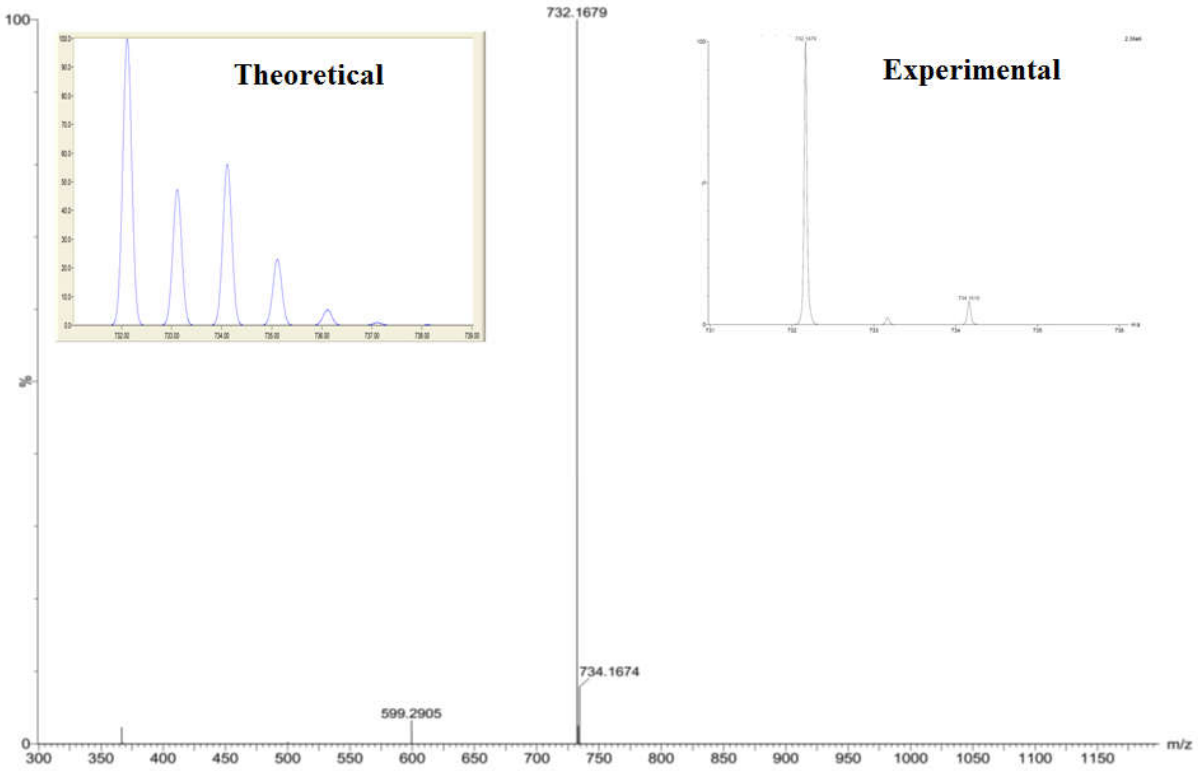

Fig. S18 ESI Mass spectrum of complex **6** in acetonitrile showing the $[M-(ClO_4^-)]^+$ peak at m/z = 732.1679. The inset shows the theoretical and experimental isotopic distributions for the complex.

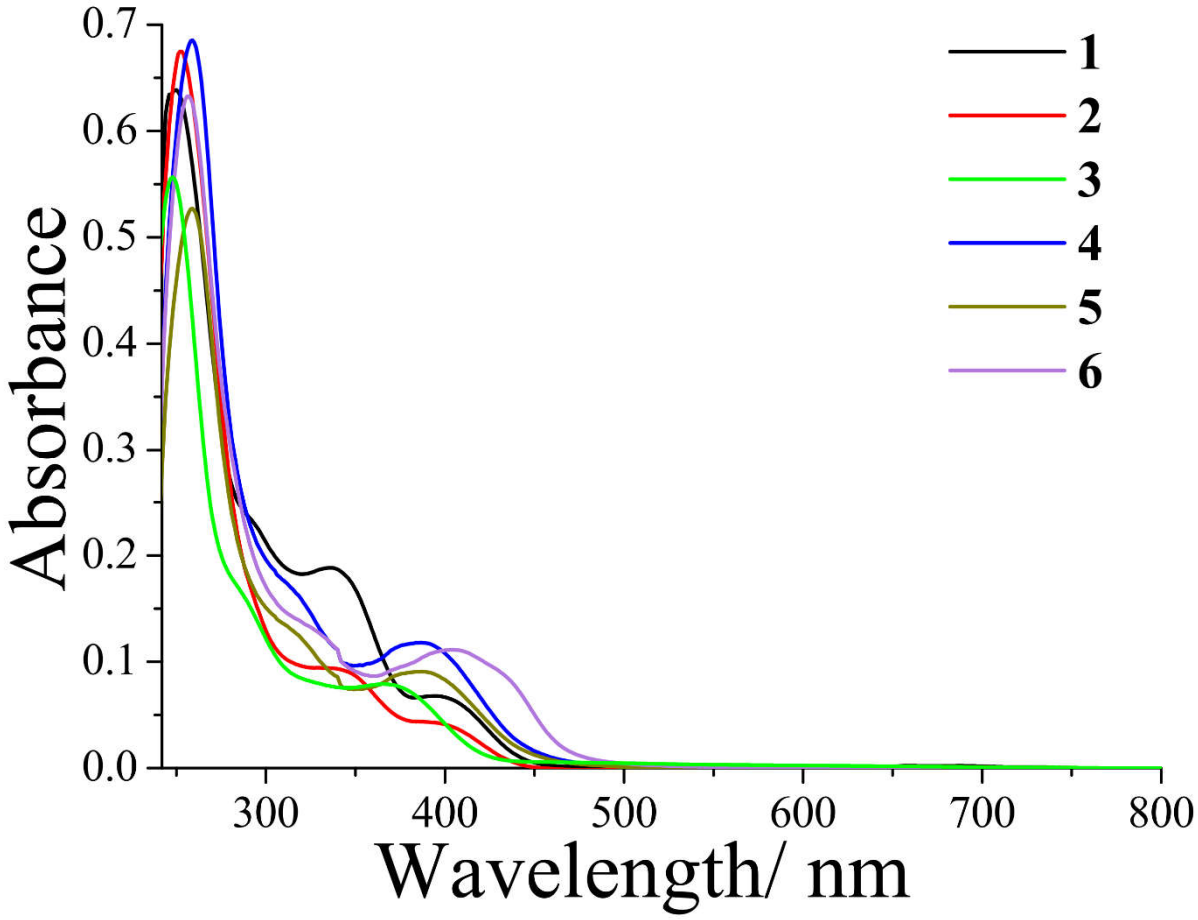

Fig. S19 UV-visible spectra of **1-6** (25 μM) in DMSO-DMEM (1:9 v/v) showing the ligand-centered bands.

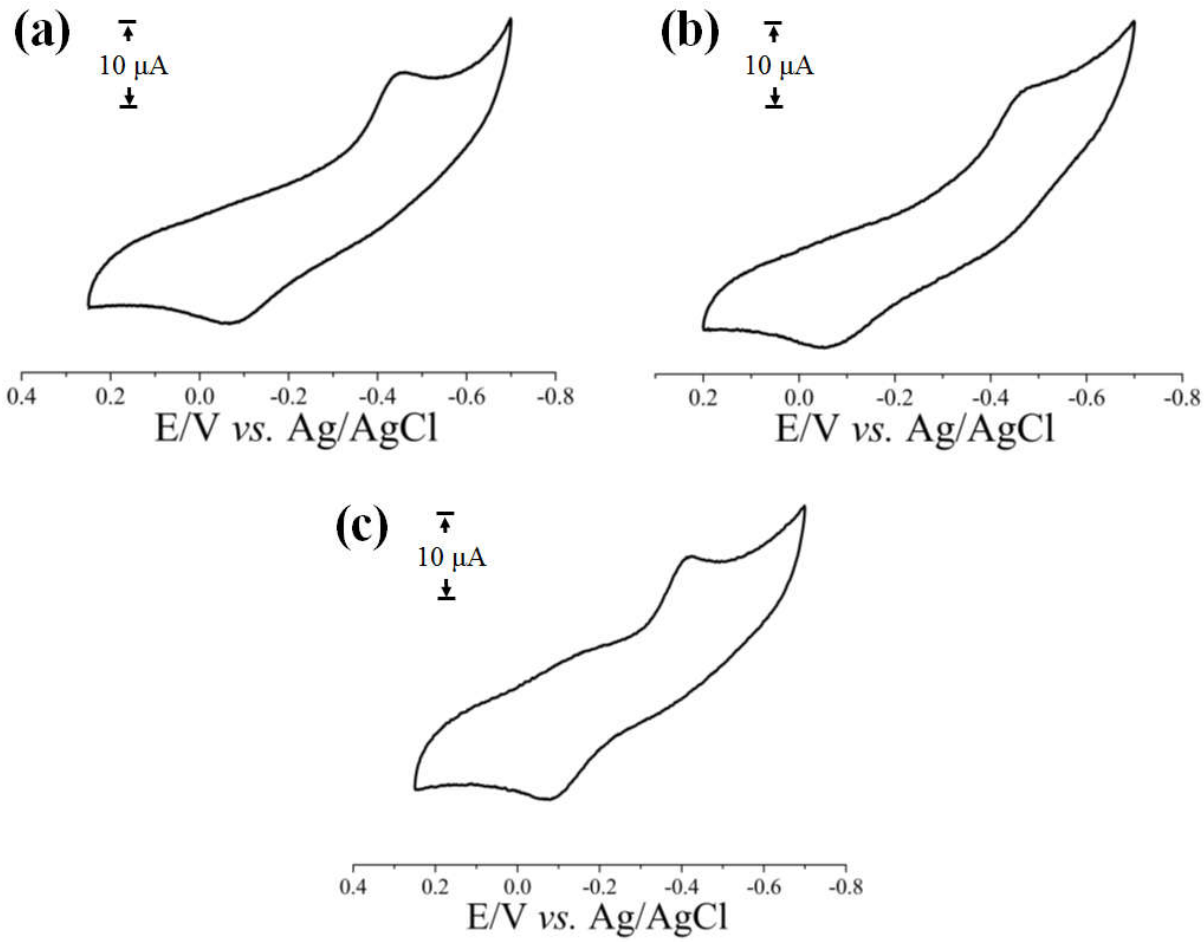

Fig. S20 Cyclic voltammetric responses of the complexes **1-3** in DMF at a scan rate of 50 mVs^{-1} using TBAP (0.1 M) as the supporting electrolyte.

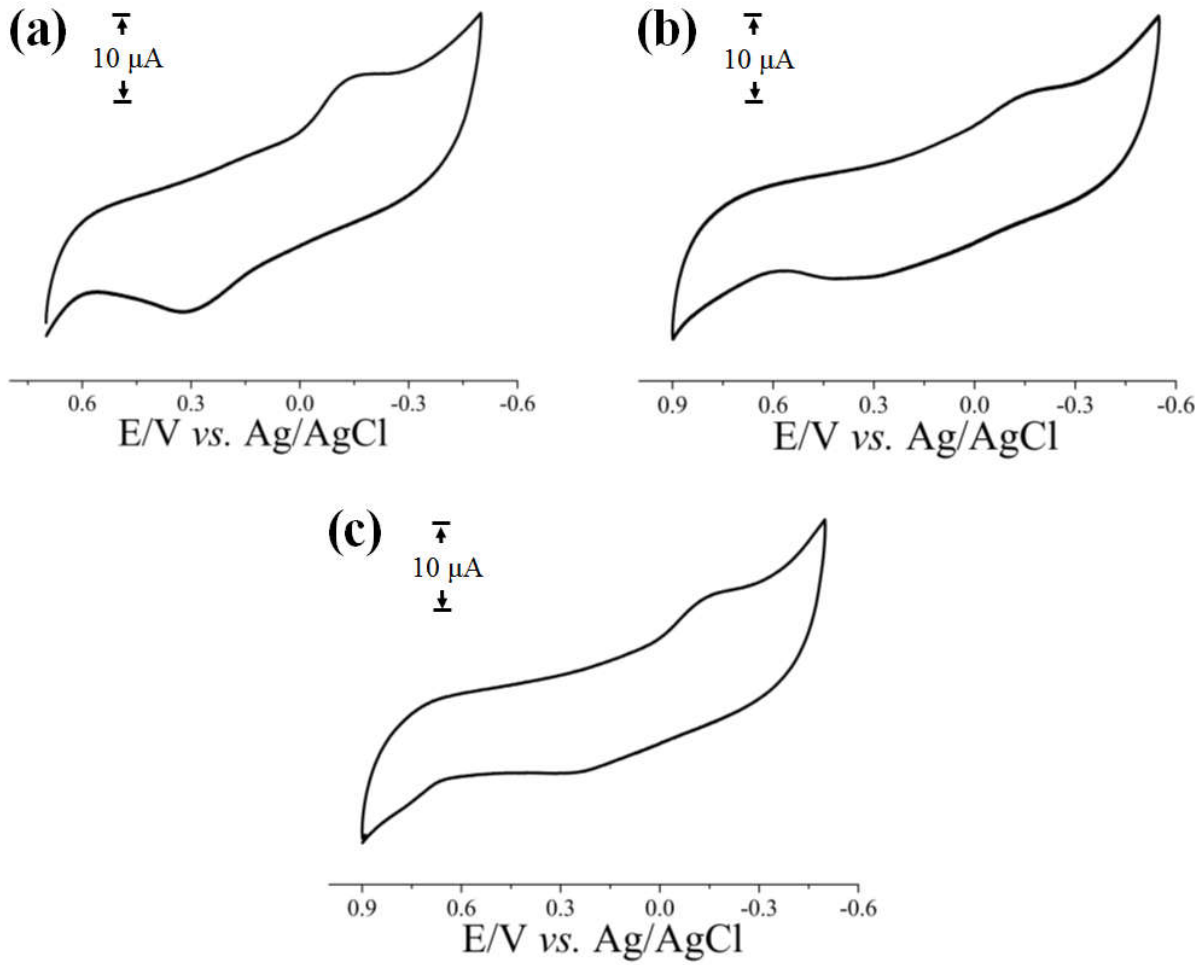

Fig. S21 Cyclic voltammetric responses of the complexes **4-6** in DMF at a scan rate of 50 mVs^{-1} using TBAP (0.1 M) as the supporting electrolyte.

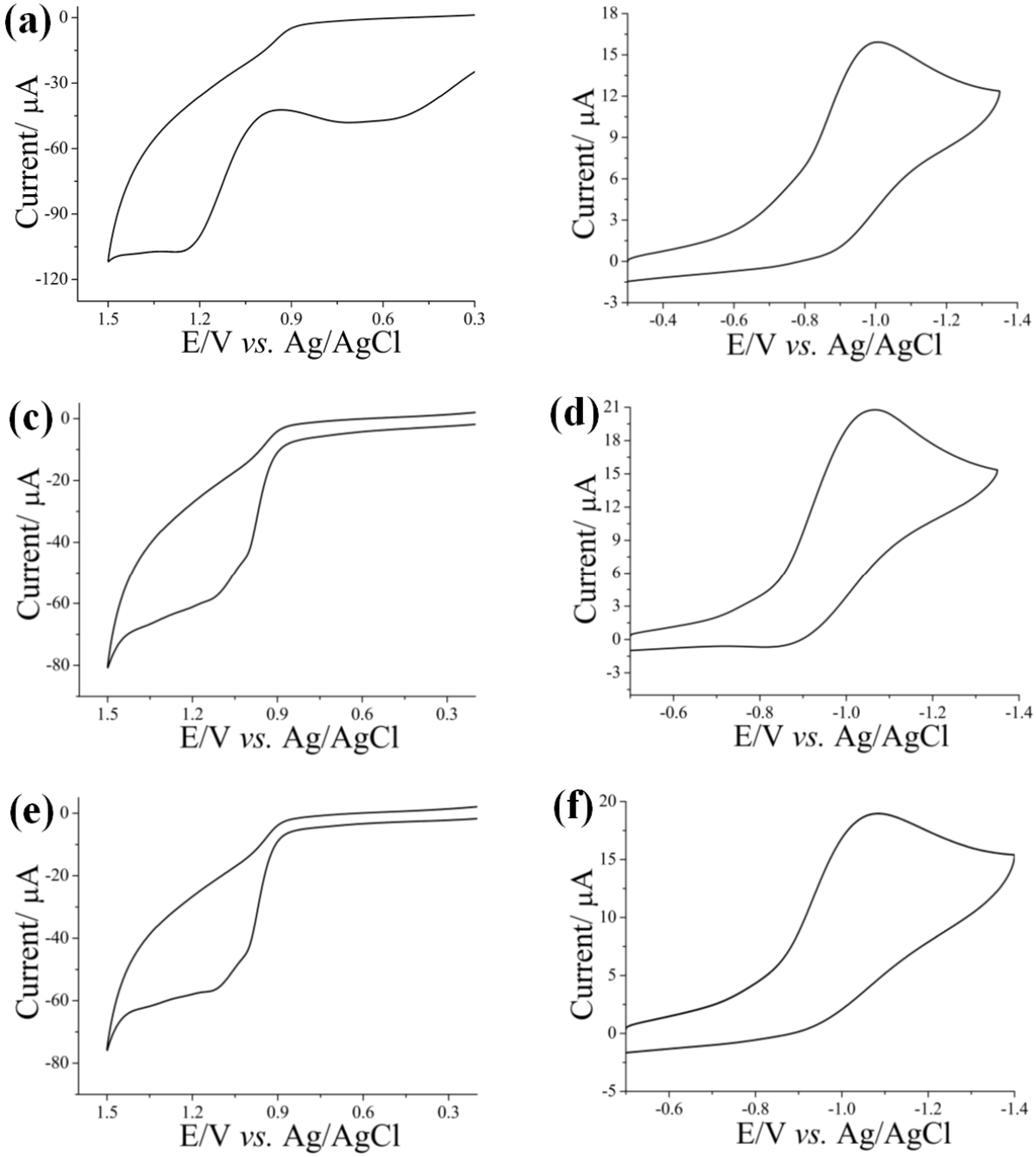

Fig. S22 Cyclic voltammetric responses of the complexes **1** (a & b), **2** (c & d) and **3** (e & f) showing the anodic and cathodic responses corresponding to the flavonoids and phenanthroline bases present in the complexes in DMF at a scan rate of 50 mVs^{-1} using TBAP (0.1 M) as the supporting electrolyte.

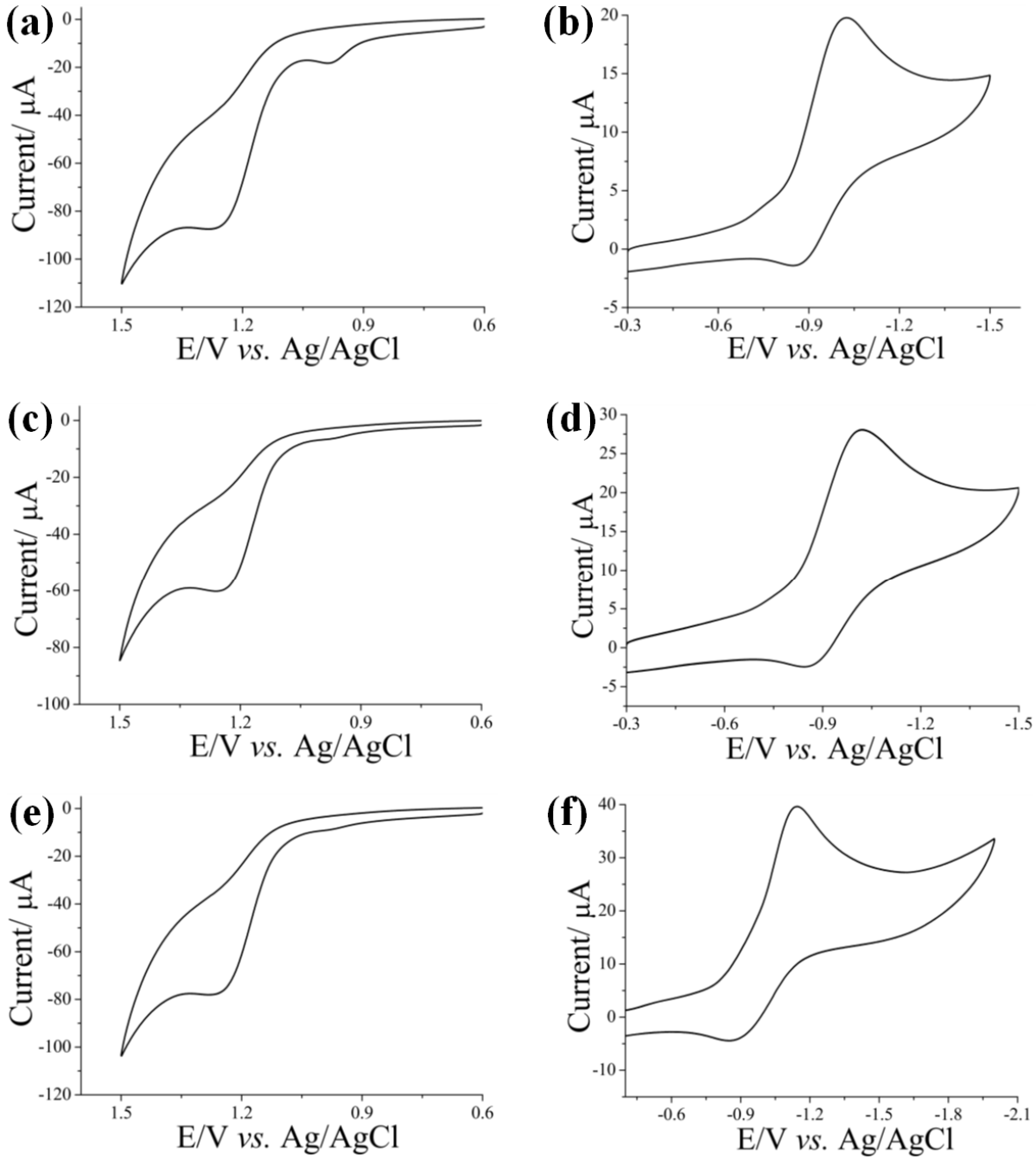

Fig. S23 Cyclic voltammetric responses of the complexes **4** (a & b), **5** (c & d) and **6** (e & f) showing the anodic and cathodic responses corresponding to the flavonoids and phenanthroline bases present in the complexes in DMF at a scan rate of 50 mVs^{-1} using TBAP (0.1 M) as the supporting electrolyte.

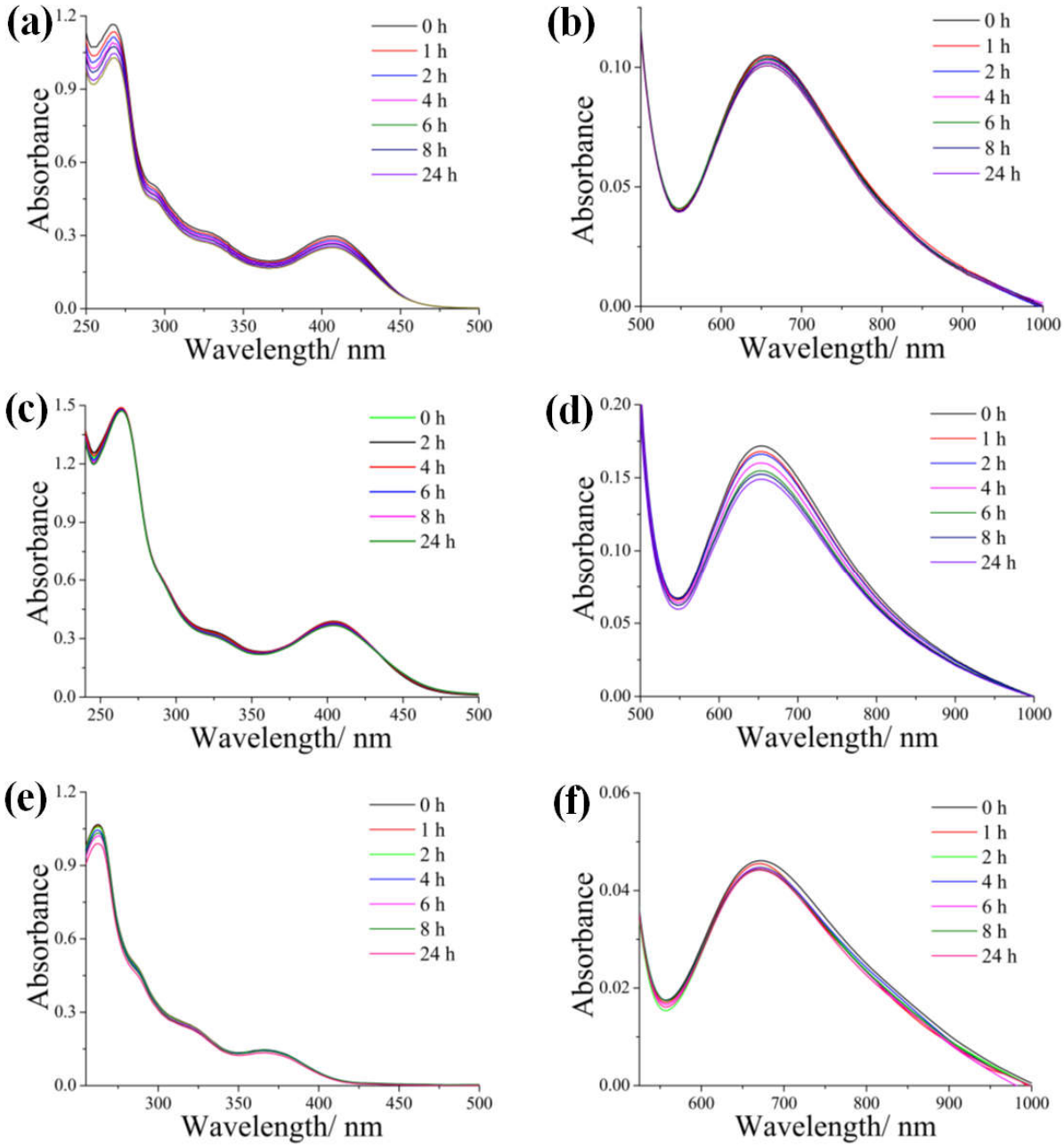

Fig. S24 UV-visible spectra of the complexes **1** (a & b), **2** (c & d) and **3** (e & f) recorded in DMSO-Tris-HCl buffer (1:9, pH 7.2) for a period of 24 h.

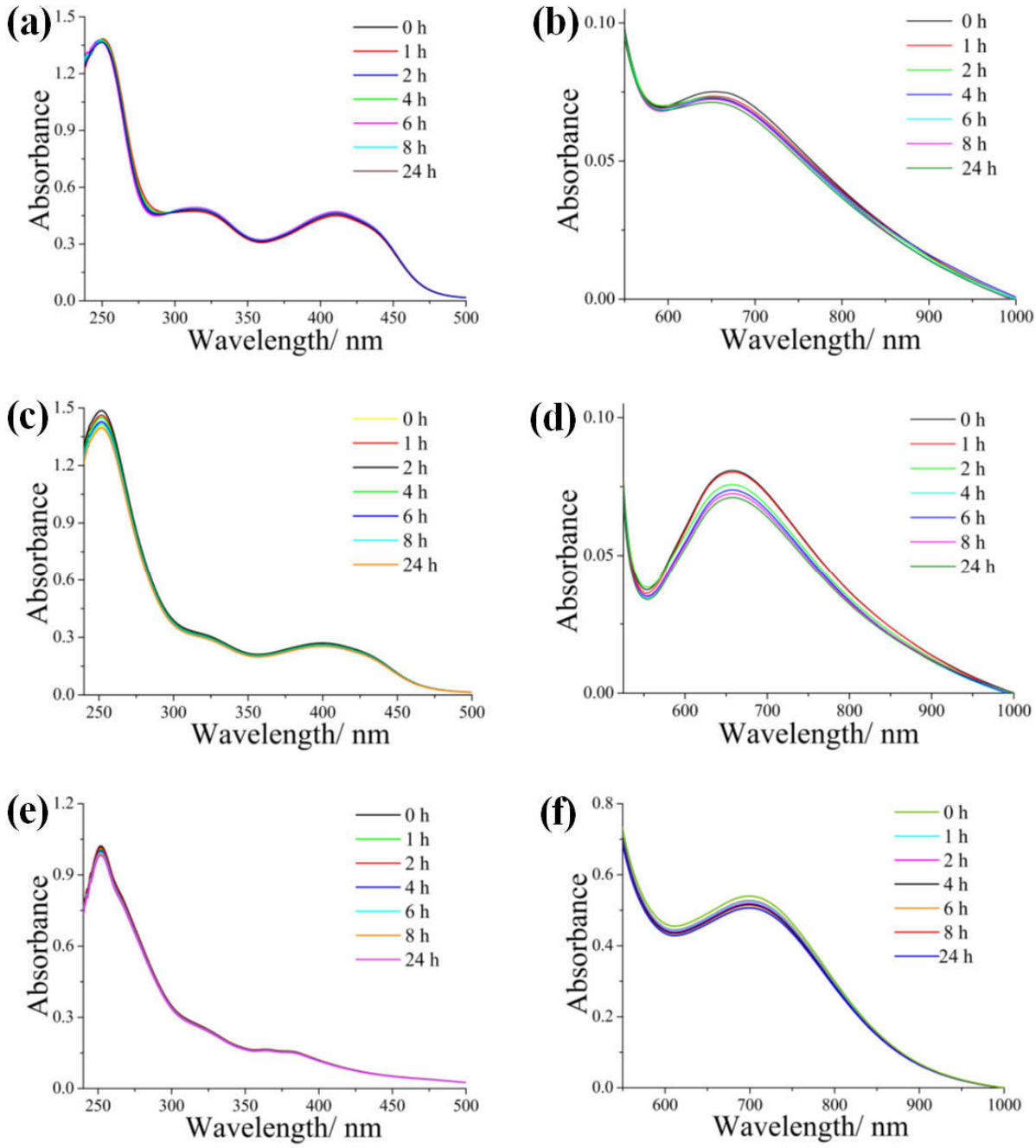

Fig. S25 UV-visible spectra of the complexes **4** (a & b), **5** (c & d) and **6** (e & f) recorded in DMSO-Tris-HCl buffer (1:9, pH 7.2) for a period of 24 h.

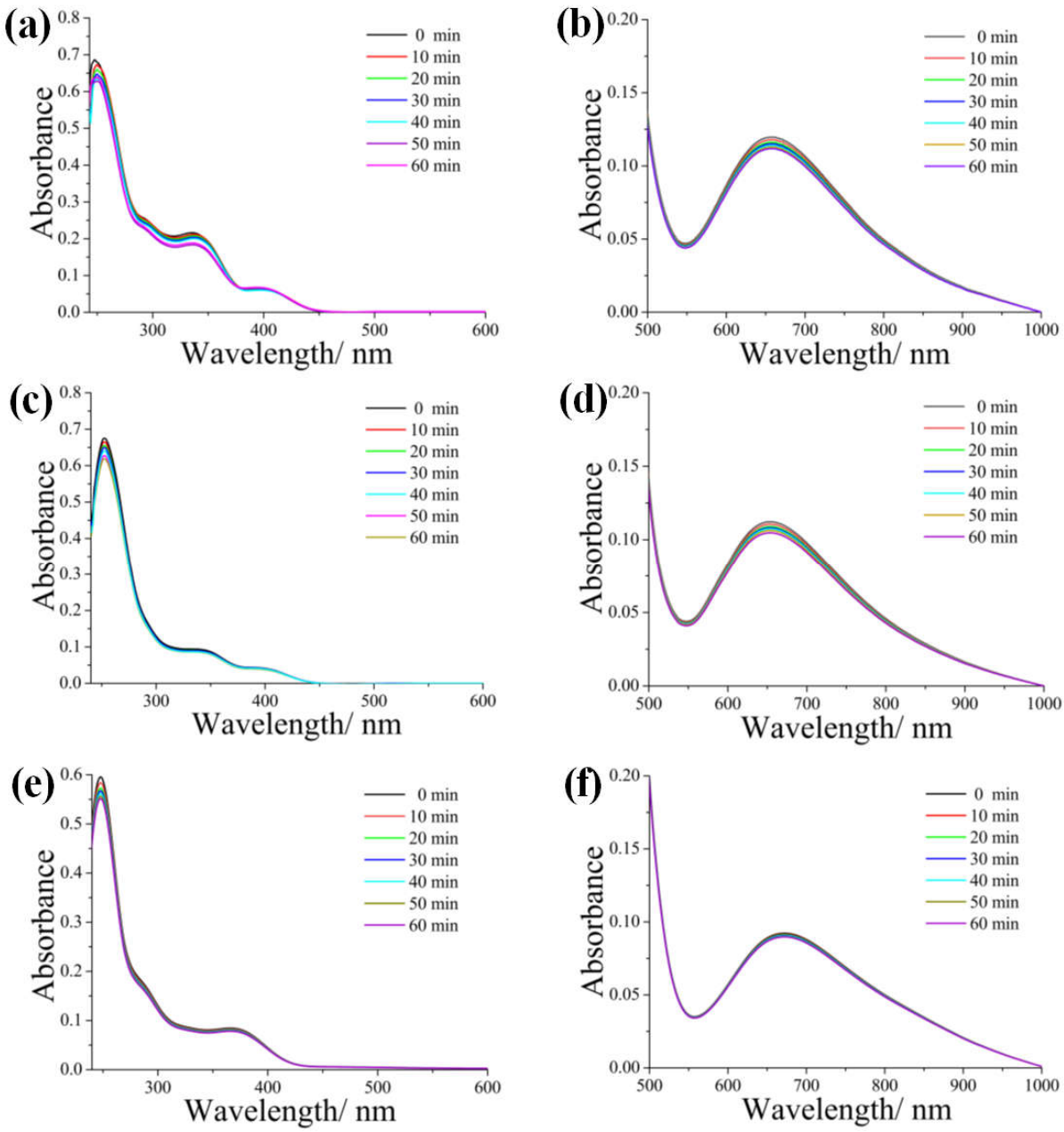

Fig. S26 UV-visible spectra of the complexes **1** (a & b), **2** (c & d) and **3** (e & f) recorded in DMSO-DMEM (1:9 v/v) showing their photostability on exposure to visible light for a period of 60 min.

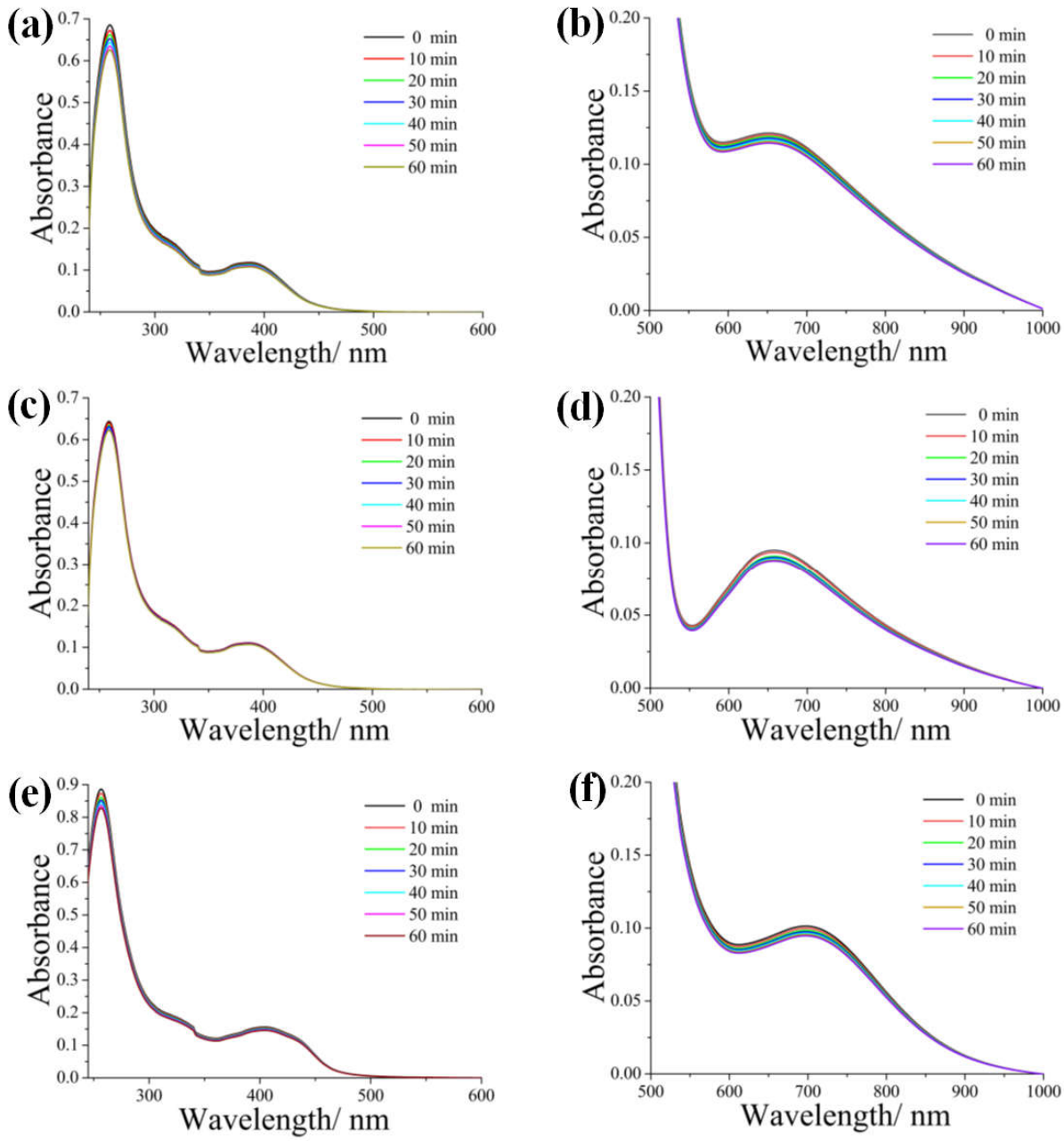

Fig. S27 UV-visible spectra of the complexes **4** (a & b), **5** (c & d) and **6** (e & f) recorded in DMSO-DMEM (1:9 v/v) showing their photostability on exposure to visible light for a period of 60 min.

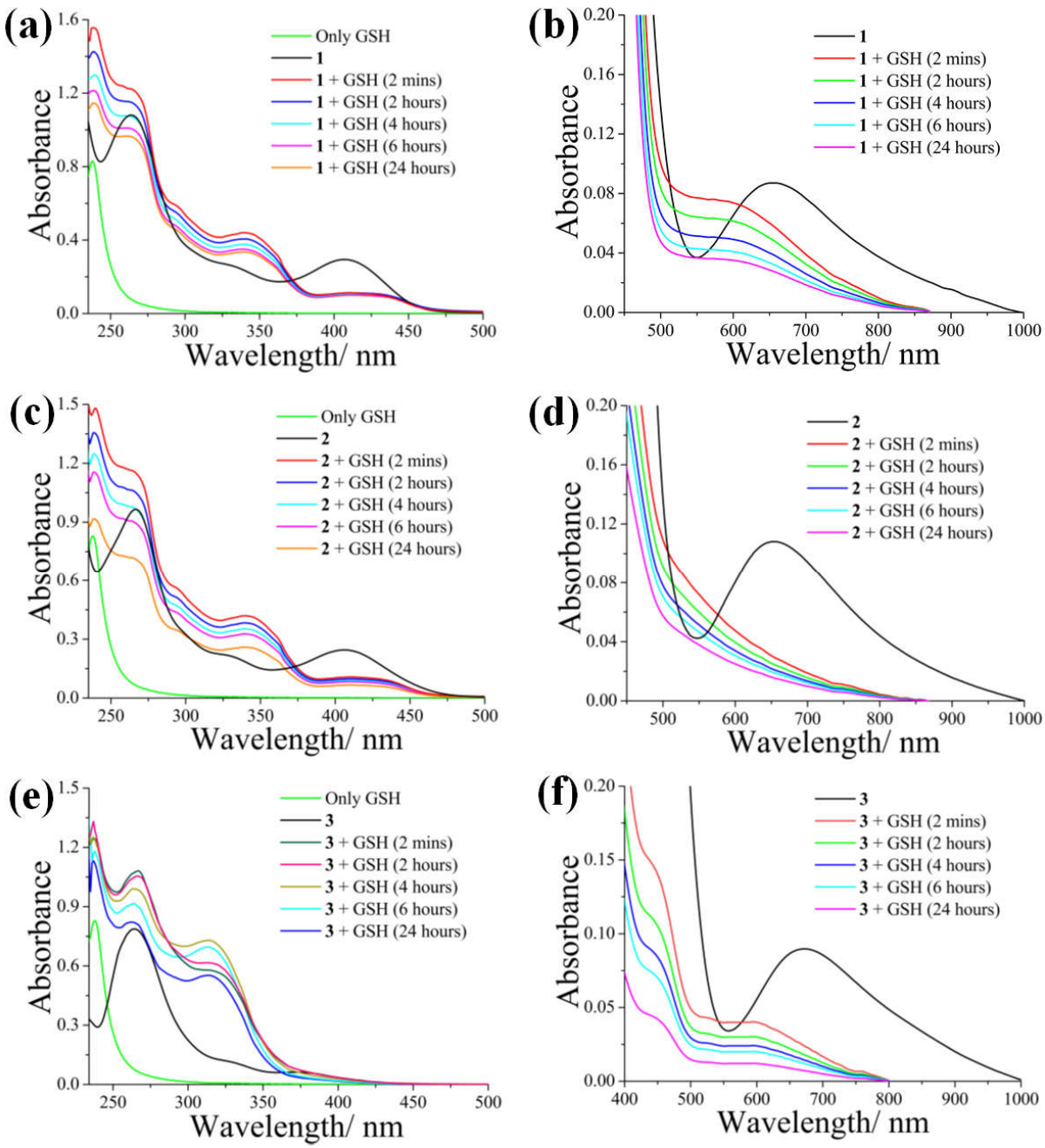

Fig. S28 UV-visible spectral changes of the complexes **1** (a & b), **2** (c & d) and **3** (e & f) recorded in DMSO-DMEM (1:9 v/v) for a period of 24 h upon treatment with GSH (3 mM).

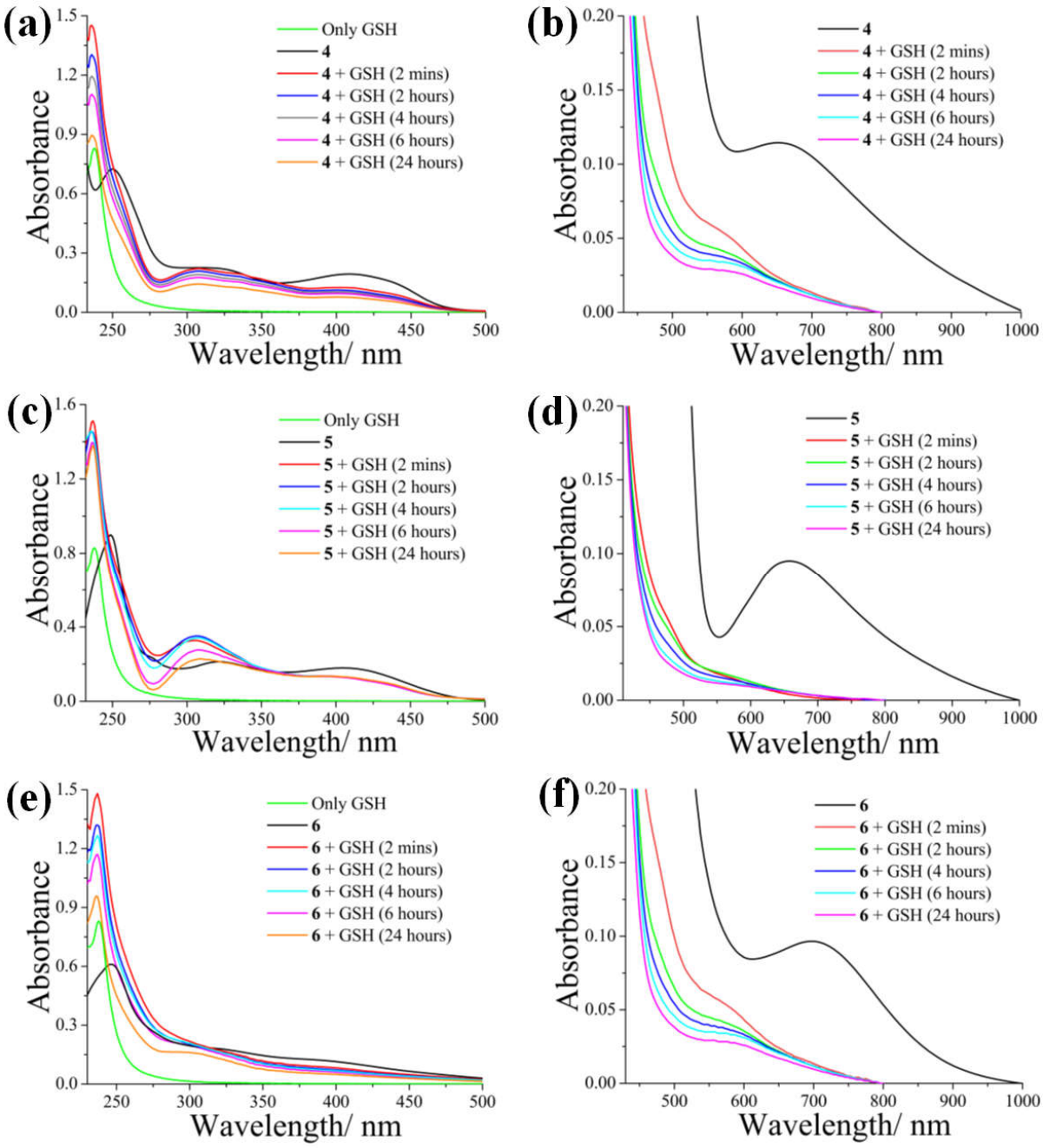

Fig. S29 UV-visible spectral changes of the complexes **4** (a & b), **5** (c & d) and **6** (e & f) recorded in DMSO-DMEM (1:9 v/v) for a period of 24 h upon treatment with GSH (3 mM).

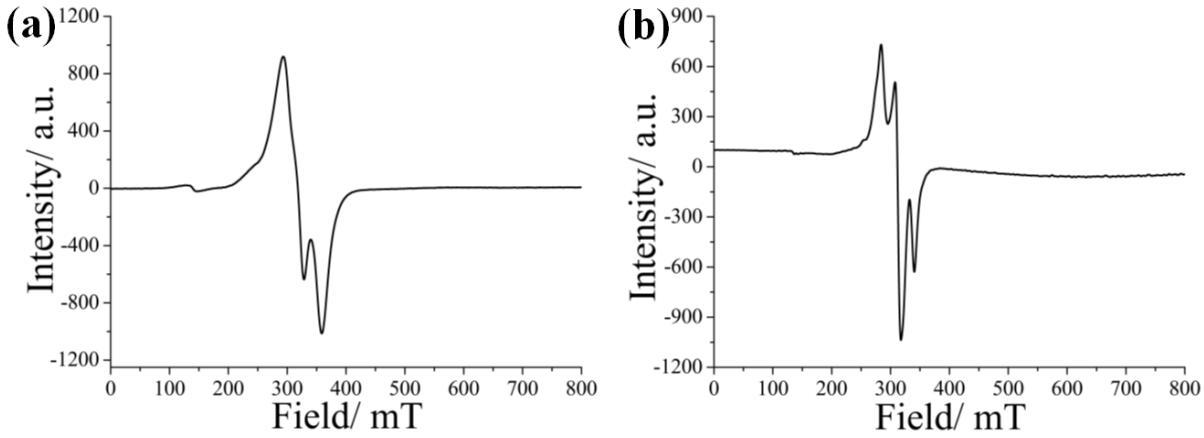

Fig. S30 EPR spectra of complex **2** in solid (a) and solution (DMSO) (b) phases at 77K.

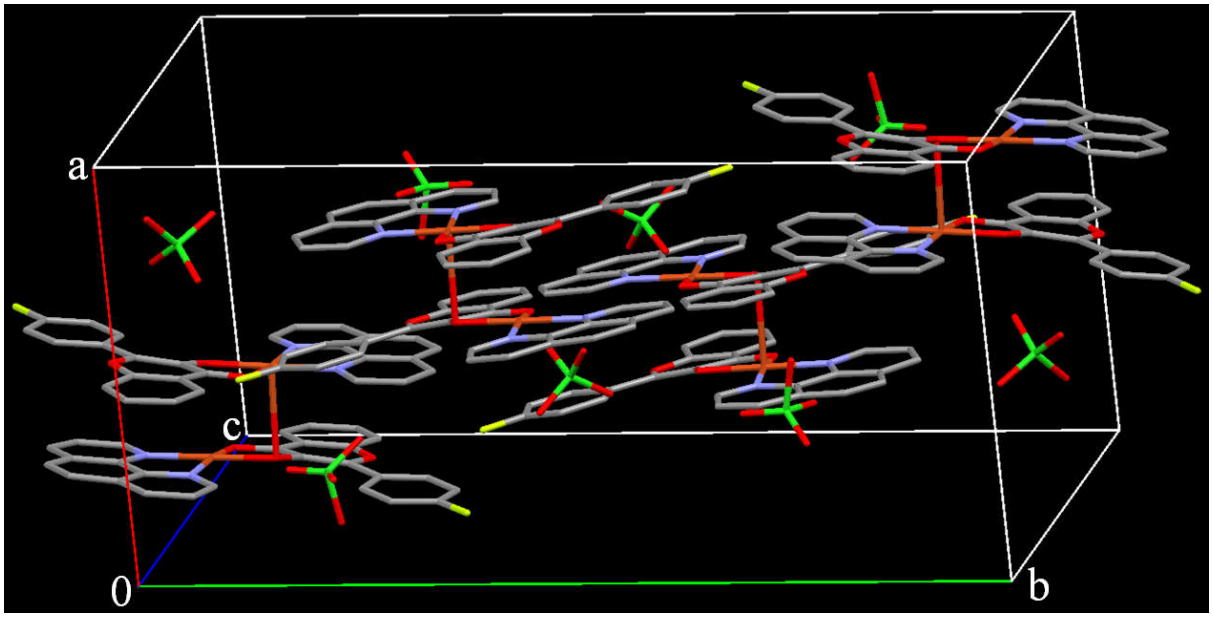

Fig. S31 Unit cell packing diagram for the complex $[Cu(L_1)(phen)](ClO_4)$ (**2**), where L_1 is monoanion of 4-fluoro-3-hydroxy flavone. The hydrogen atoms are omitted for clarity.

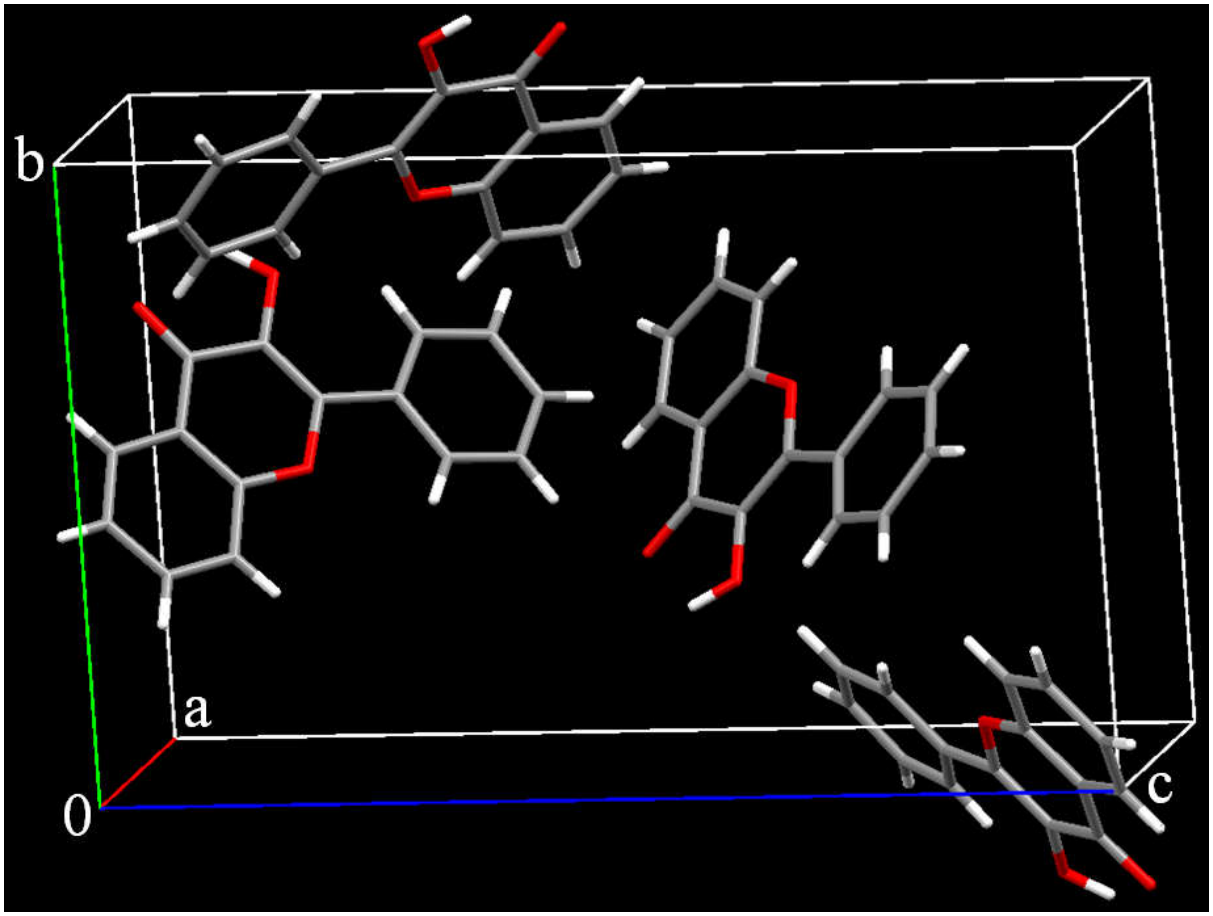

Fig. S32 Unit cell packing diagram of ligand 3-hydroxy flavone.

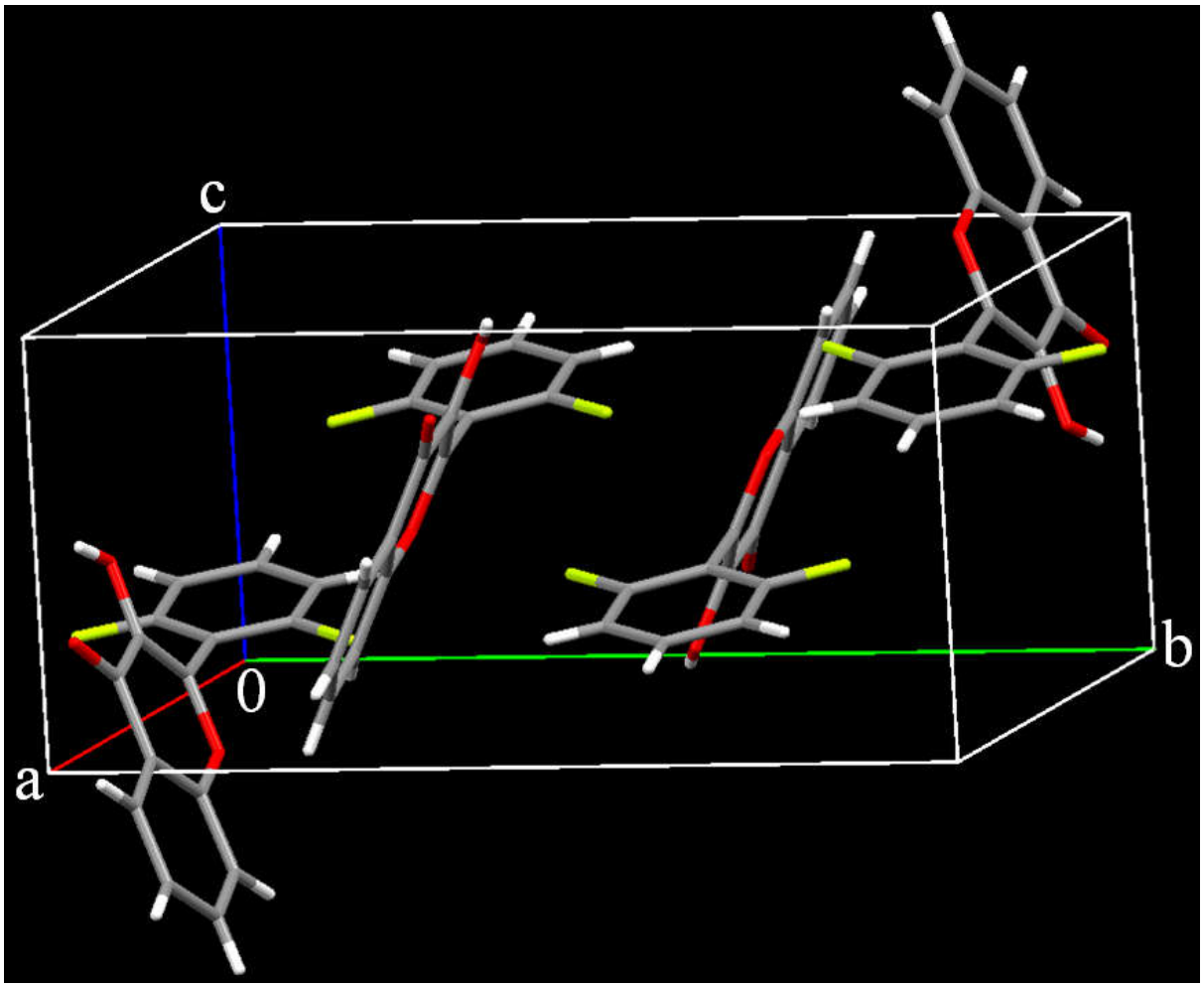

Fig. S33 Unit cell packing diagram of ligand 2,6-difluoro-3-hydroxy flavone.

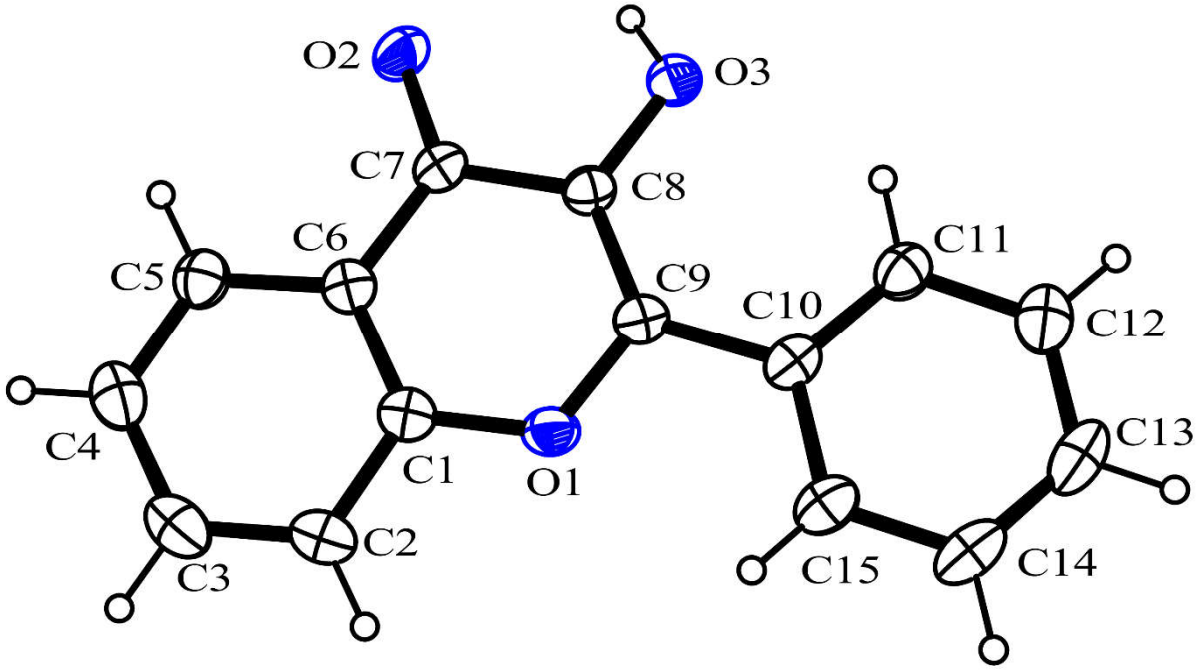

Fig. S34 ORTEP view of the ligand 3-hydroxy flavone showing 30% probability thermal ellipsoids.

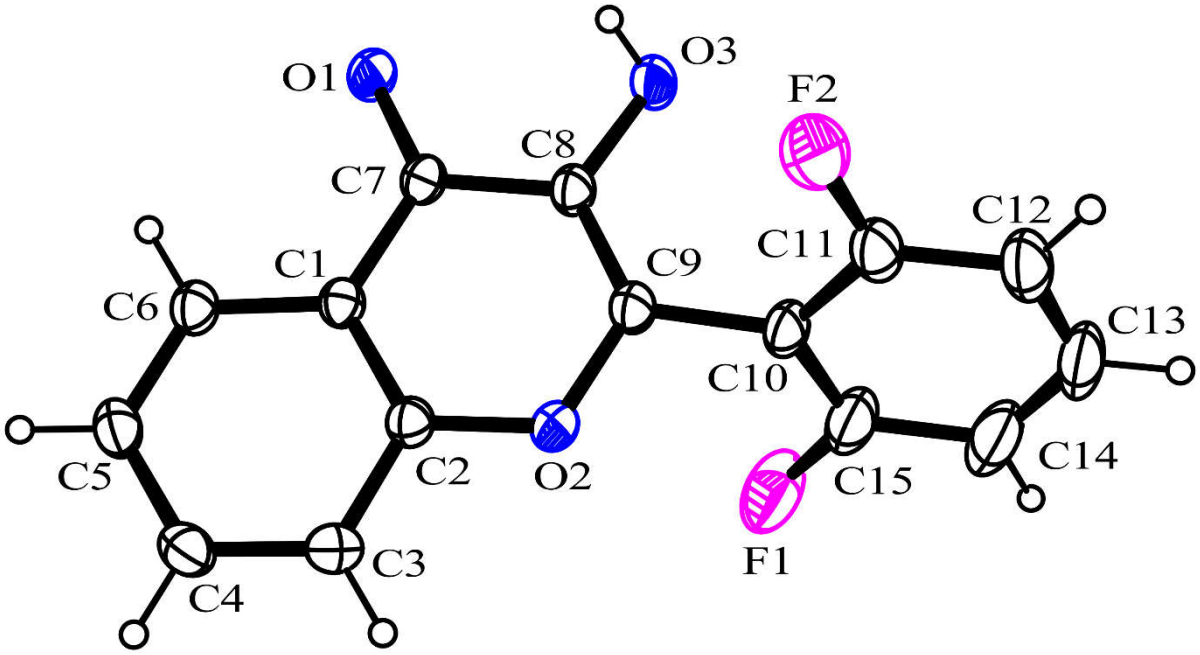

Fig. S35 ORTEP view of the ligand 2,6-difluoro-3-hydroxy flavone showing 30% probability thermal ellipsoids.

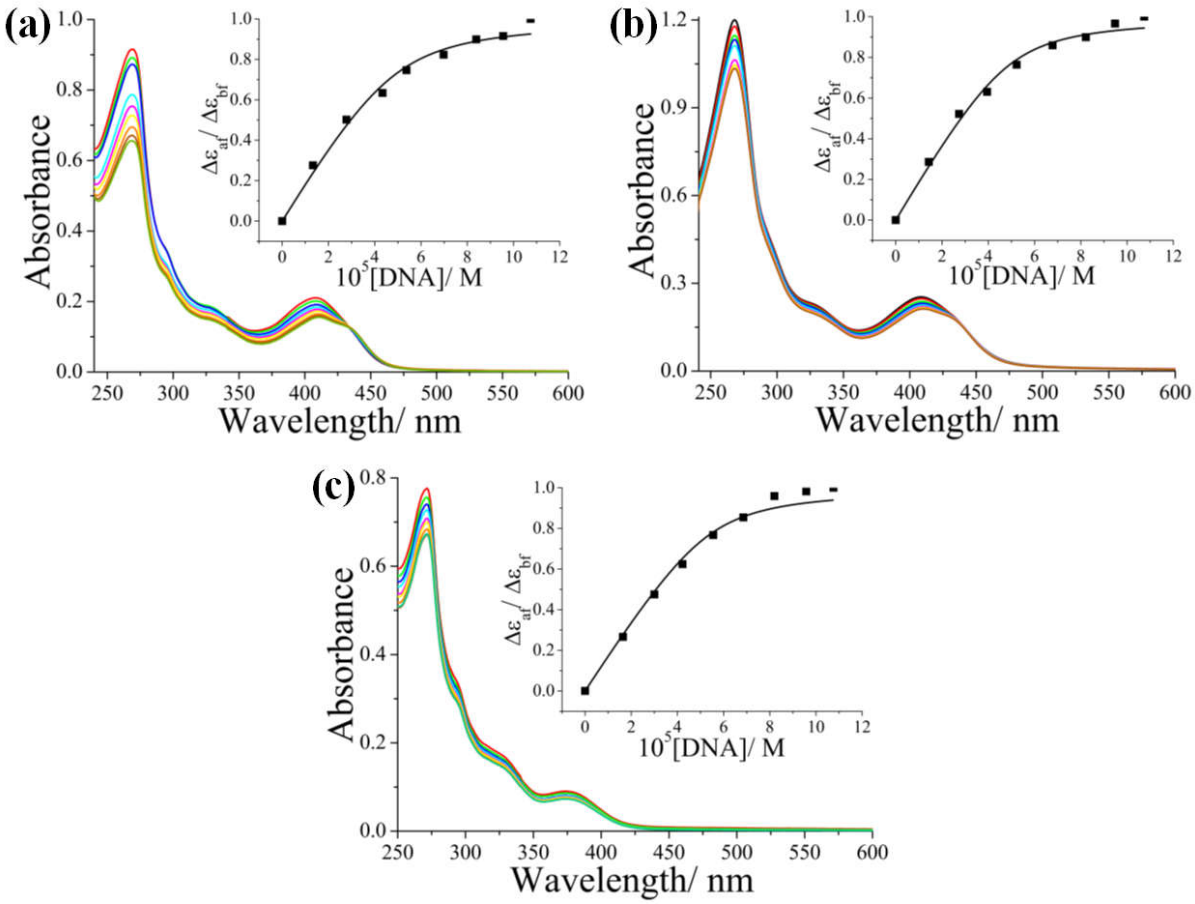

Fig. S36 Absorption spectral traces of the complexes **1-3** (a-c) in 5 mM Tris-HCl buffer (pH 7.2) on increasing the quantity of calf thymus DNA. The inset shows the least square fits of $\Delta\varepsilon_{af}/\Delta\varepsilon_{bf}$ *vs.* [DNA] for the complexes using McGhee-von Hippel (MvH) method.

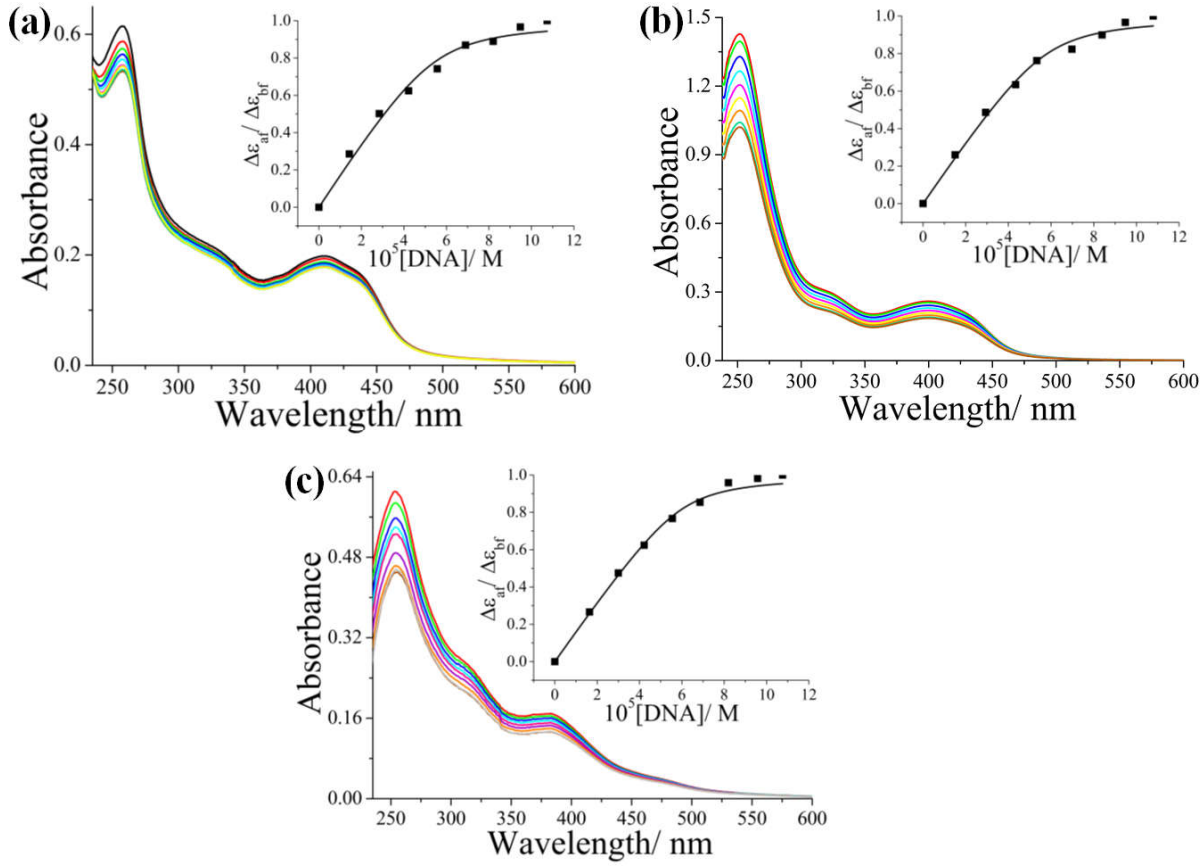

Fig. S37 Absorption spectral traces of the complexes **4-6** (a-c) in 5 mM Tris-HCl buffer (pH 7.2) on increasing the quantity of calf thymus DNA. The inset shows the least square fits of $\Delta\varepsilon_{af}/\Delta\varepsilon_{bf}$ *vs.* [DNA] for the complexes using McGhee-von Hippel (MvH) method.

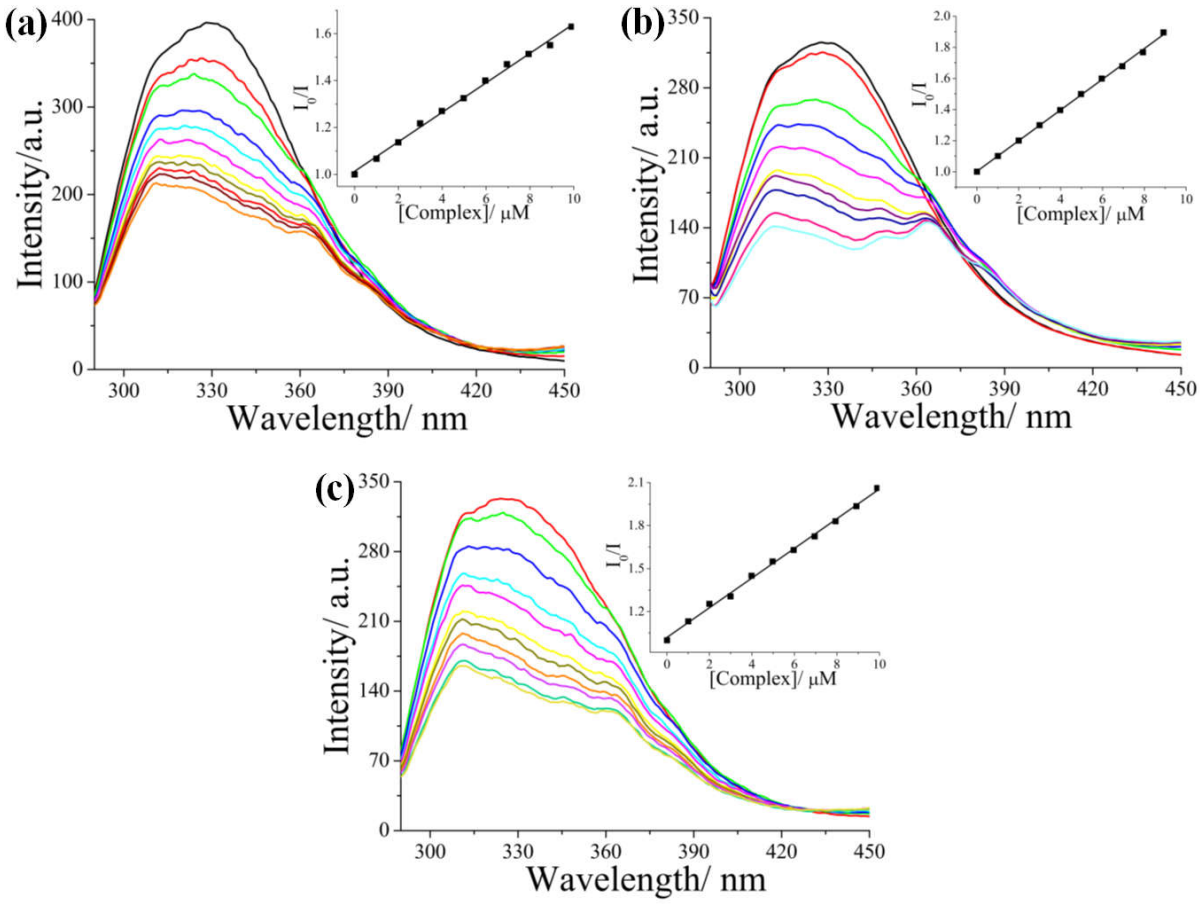

Fig. S38 Emission spectral traces of HSA (2 μM) in the presence of complexes **1-3** (a-c). The inset shows the plot of (I_0/I) *vs.* [complex].

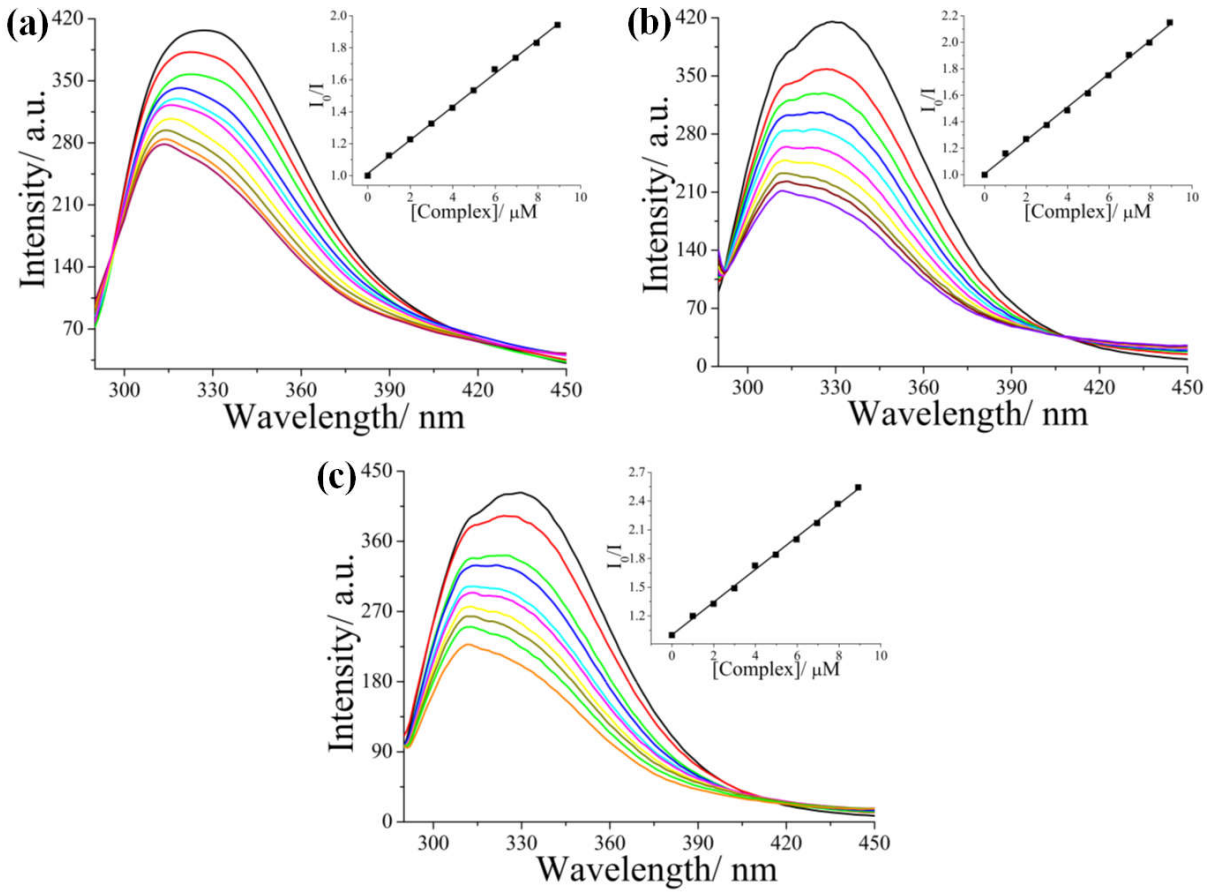

Fig. S39 Emission spectral traces of HSA (2 μM) in the presence of complexes **4-6** (a-c). The inset shows the plot of (I_0/I) *vs.* [complex].

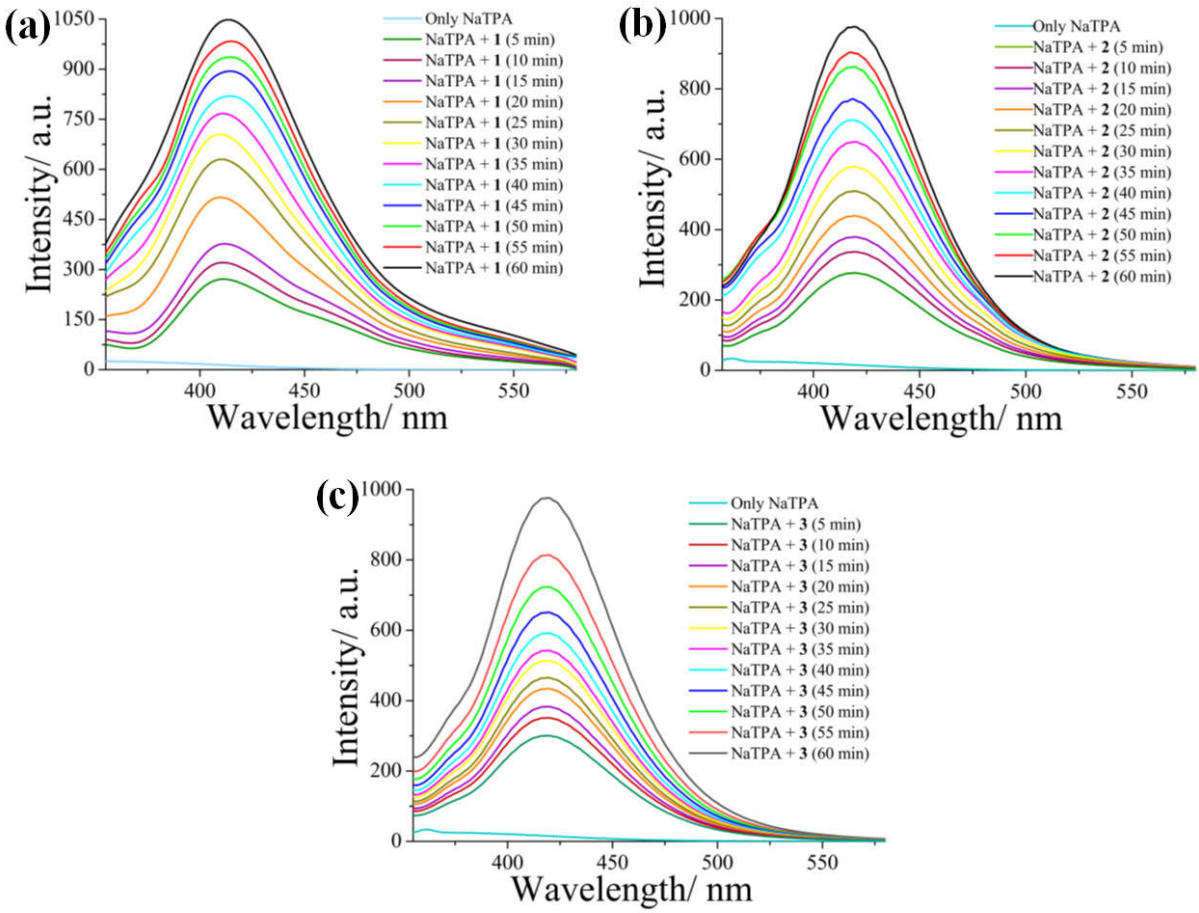

Fig. S40 Fluorescence spectra of HTA solution resulting from the reaction of TA (2 mM) with •OH radical generated by the complexes (a) **1**, (b) **2** and (c) **3** (25 μM) on exposure to visible light for different time interval.

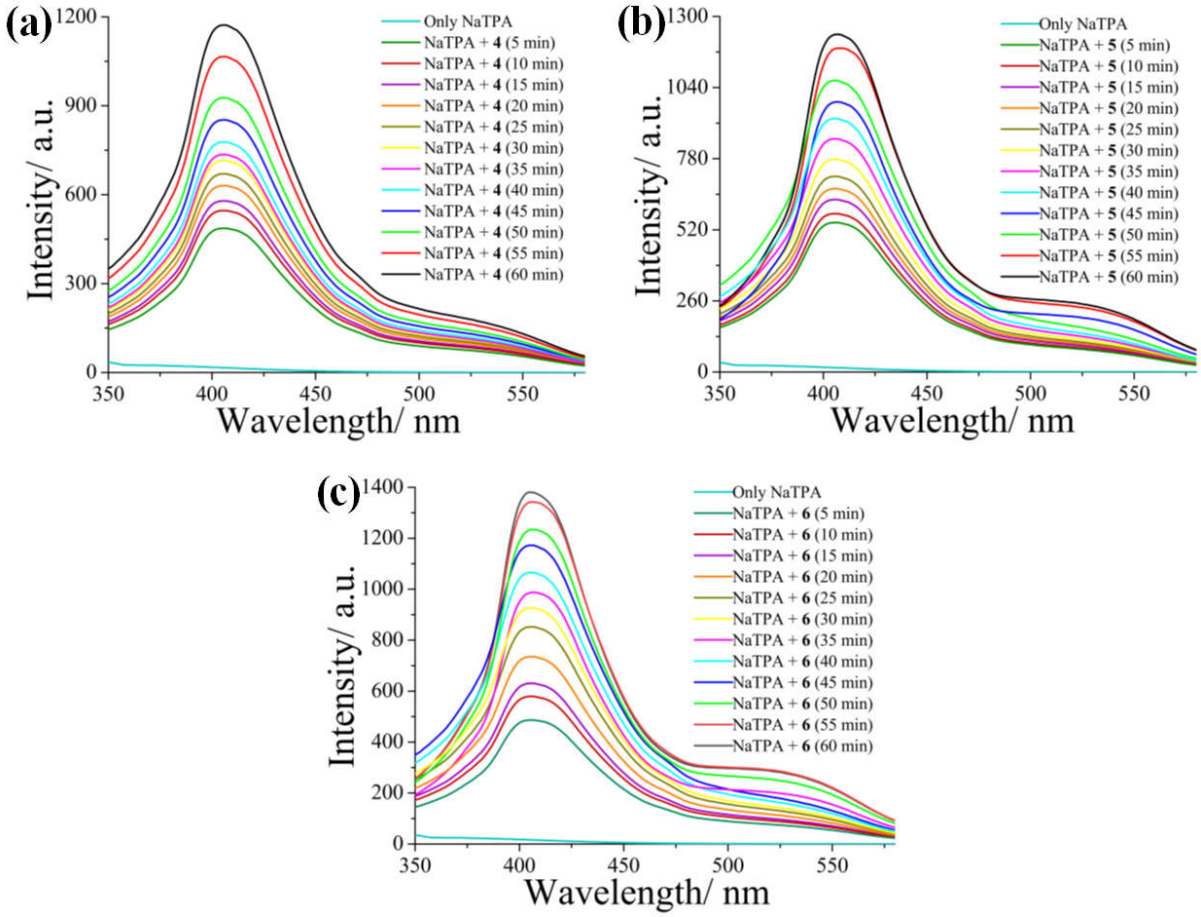

Fig. S41 Fluorescence spectra of HTA solution resulting from the reaction of TA (2 mM) with •OH radical generated by the complexes (a) **4**, (b) **5** and (c) **6** (25 μM) on exposure to visible light for different time interval.

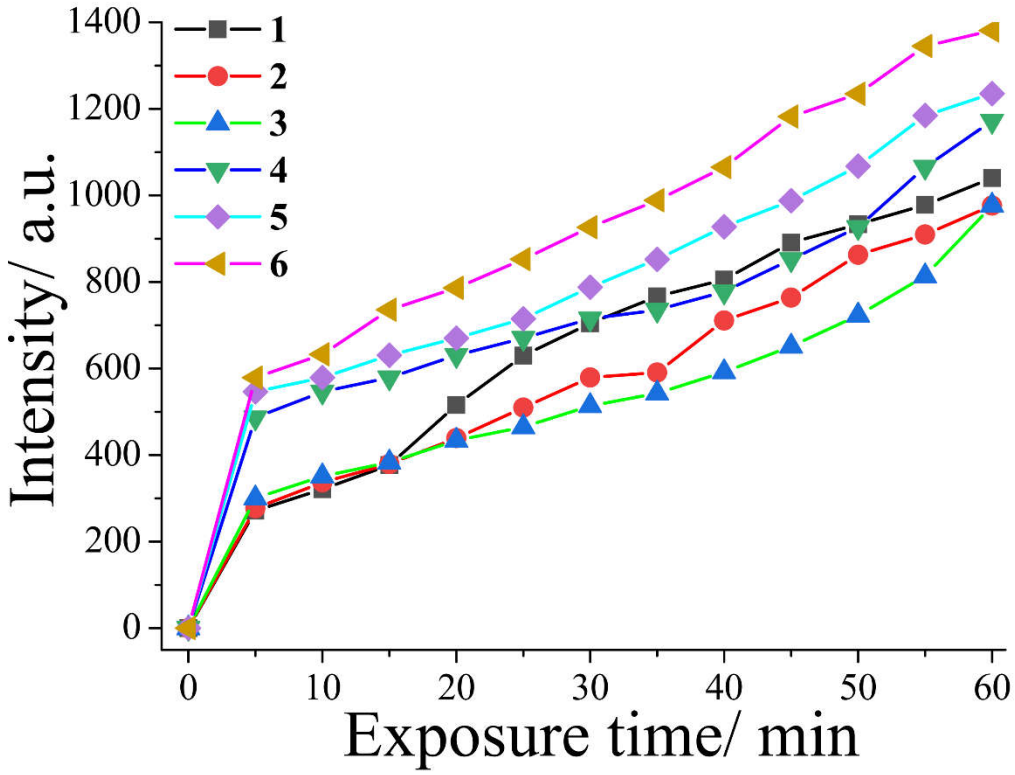

Fig. S42 A comparison of the increase in concentration of HTA from the reaction of TA (2 mM) with •OH radical generated by the complexes **1-6** (25 μM) on exposure to visible light for different time interval.

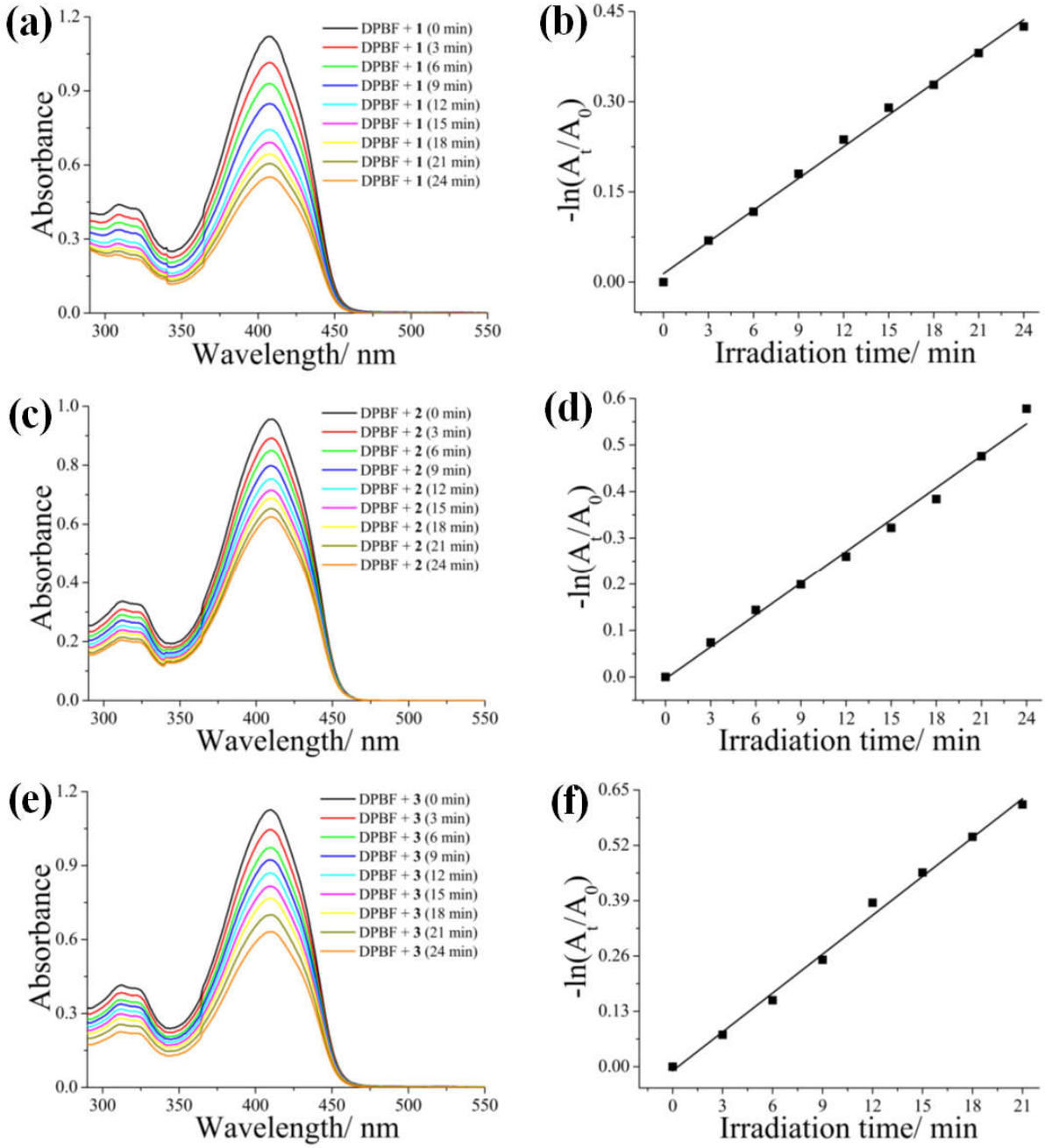

Fig. S43 Absorption spectral traces of 1,3-diphenylisobenzofuran (DPBF) (1 mM) in presence of complexes (a) **1**, (c) **2** and (e) **3** (25 μM) on visible light irradiation for different time interval indicating generation of $^1O_2$. The panels (b) **1**, (d) **2** and (f) **3** show the first-order plot of absorbance of DPBF versus irradiation time for the complexes.

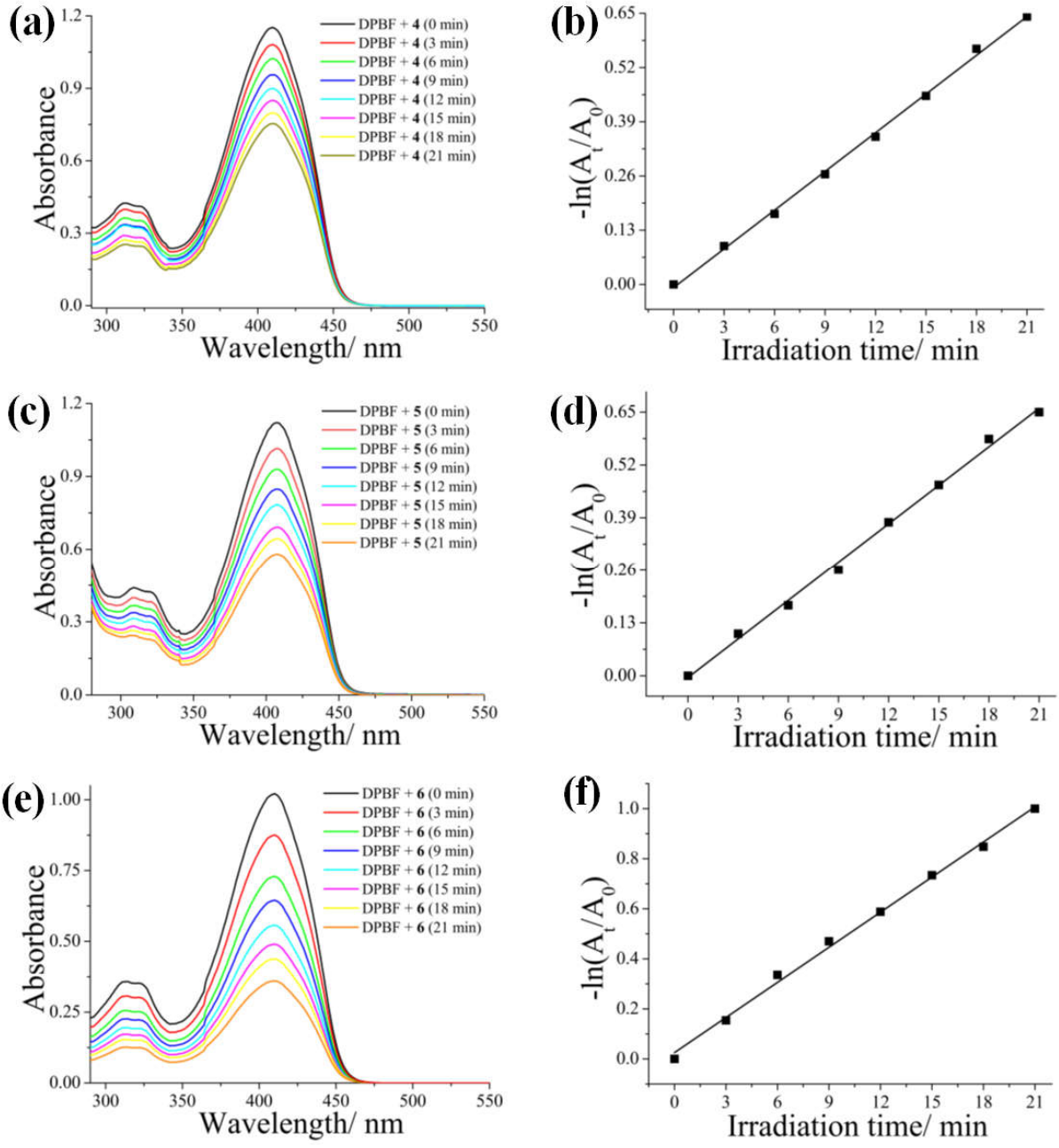

Fig. S44 Absorption spectral traces of 1,3-diphenylisobenzofuran (DPBF) (1 mM) in presence of complexes (a) **4**, (c) **5** and (e) **6** (25 μM) on visible light irradiation for different time interval indicating generation of $^1O_2$. The panels (b) **4**, (d) **5** and (f) **6** show the first-order plot of absorbance of DPBF versus irradiation time for the complexes.

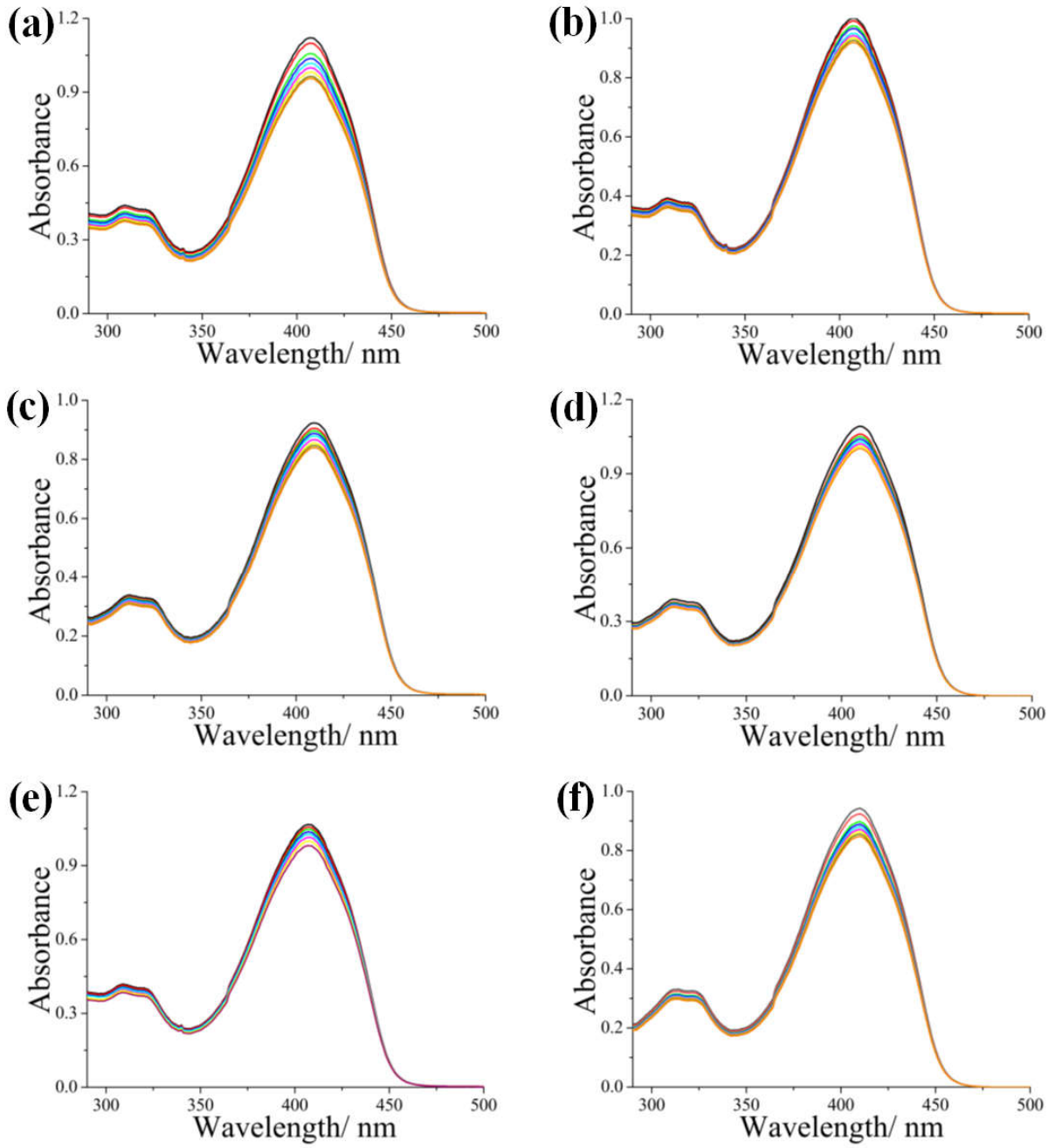

Fig. S45 Absorption spectral traces of 1,3-diphenylisobenzofuran (DPBF) (1 mM) in presence of complexes (a) **1**, (b) **2**, (c) **3**, (d) **4**, (e) **5** and (e) **6** (25 μM) in dark at different time interval indicating that there is no significant generation of $^1O_2$.

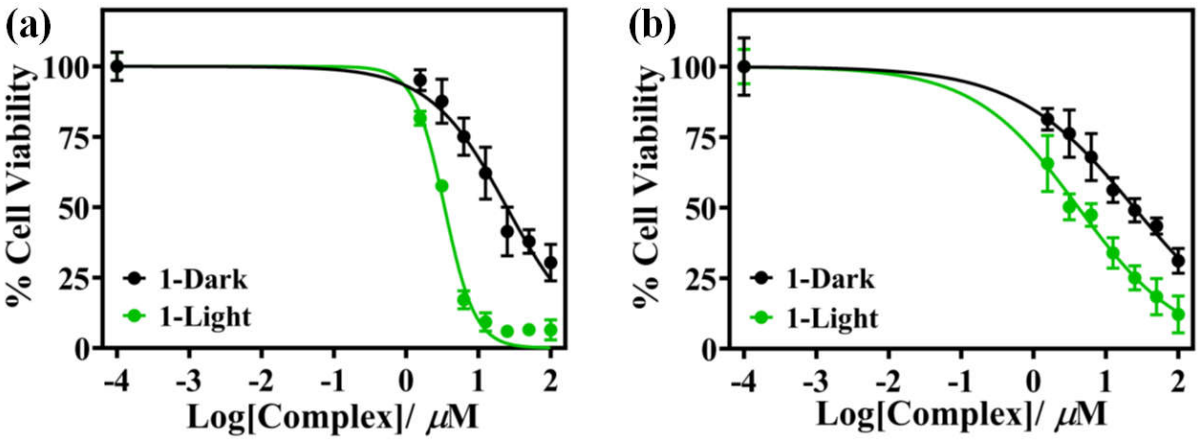

Fig. S46 Cell viability plots showing the cytotoxic effect of complex **1** in (a) MCF-7 and (b) A549 cells in dark (black) and in the presence of visible light (green, 400-700 nm, 10 J cm^{-2}, 1 h).

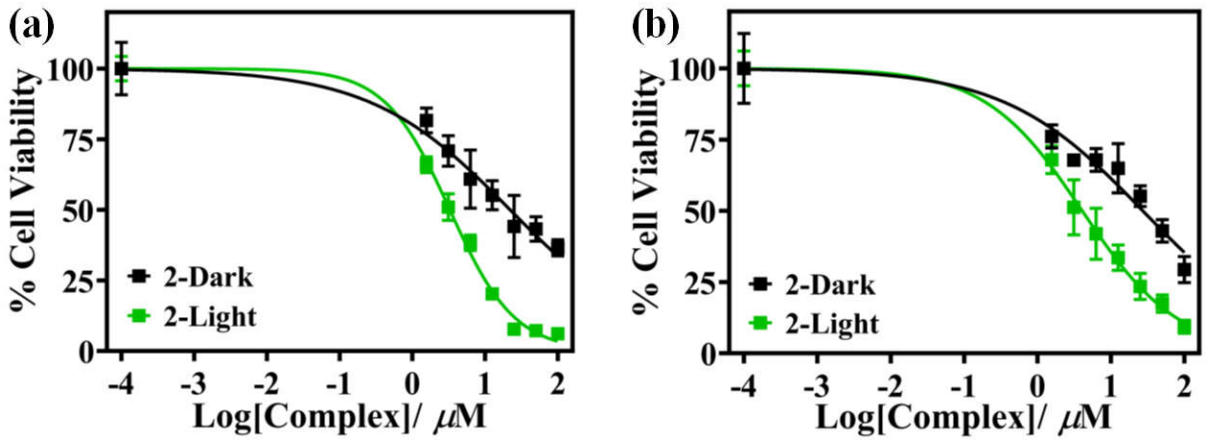

Fig. S47 Cell viability plots showing the cytotoxic effect of complex **2** in (a) MCF-7 and (b) A549 cells in dark (black) and in the presence of visible light (green, 400-700 nm, 10 J cm^{-2}, 1 h).

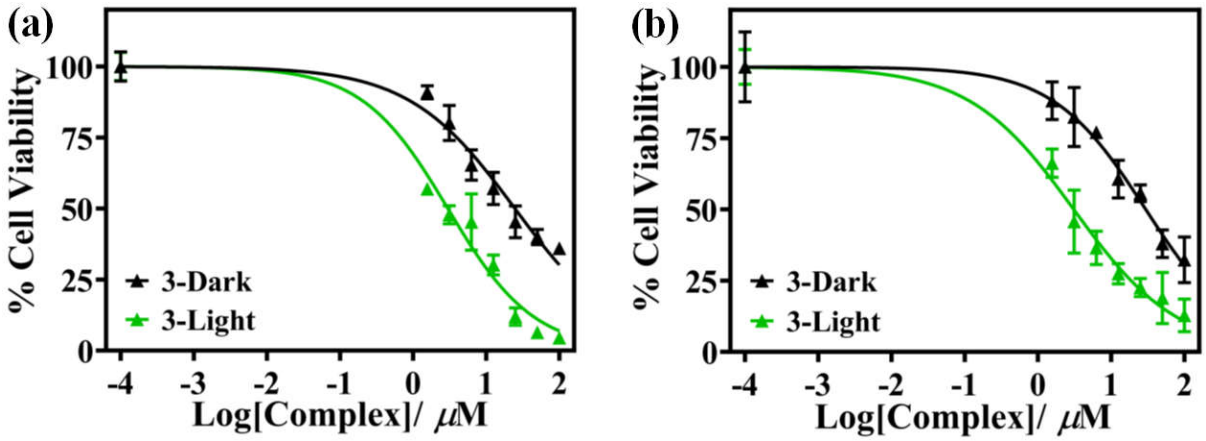

Fig. S48 Cell viability plots showing the cytotoxic effect of complex **3** in (a) MCF-7 and (b) A549 cells in dark (black) and in the presence of visible light (green, 400-700 nm, 10 J cm^{-2}, 1 h).

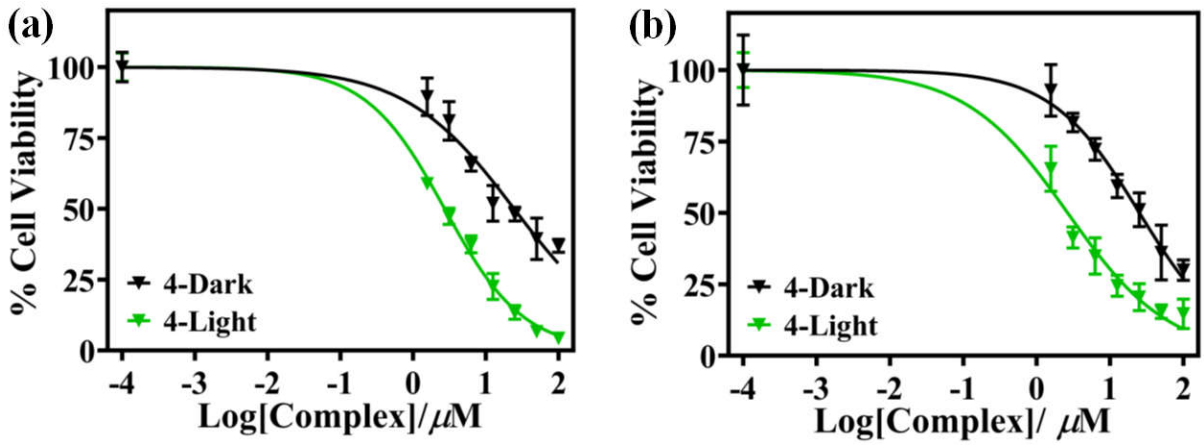

Fig. S49 Cell viability plots showing the cytotoxic effect of complex **4** in (a) MCF-7 and (b) A549 cells in dark (black) and in the presence of visible light (green, 400-700 nm, 10 J cm^{-2}, 1 h).

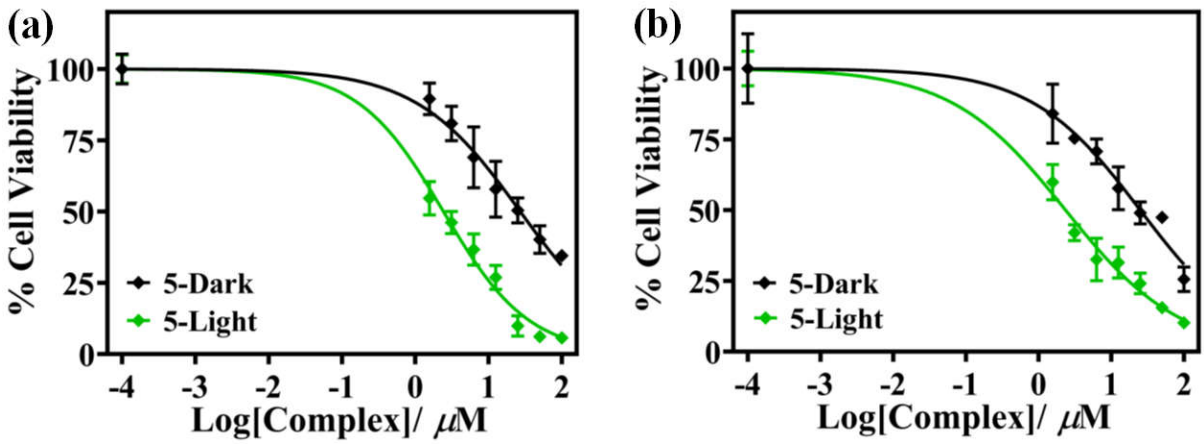

Fig. S50 Cell viability plots showing the cytotoxic effect of complex **5** in (a) MCF-7 and (b) A549 cells in dark (black) and in the presence of visible light (green, 400-700 nm, 10 J cm^{-2}, 1 h).

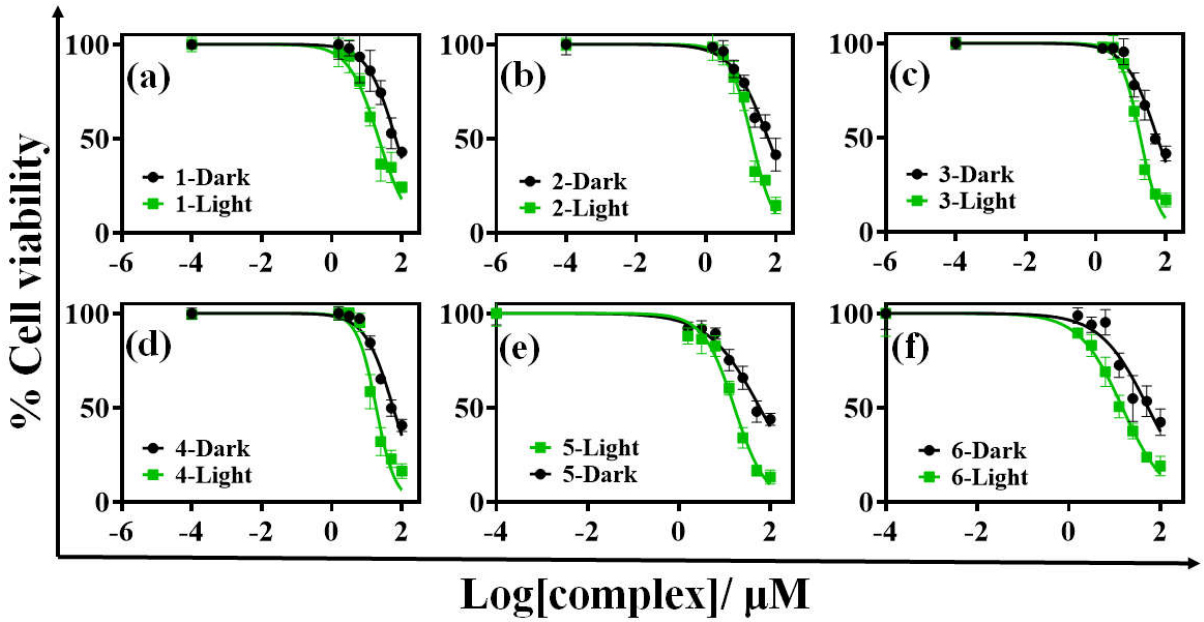

Fig. S51 Cell viability plots showing the cytotoxic effect of the complexes **1-6** in HPL1D cells in dark (black) and in the presence of visible light (green, 400-700 nm, 10 J cm^{-2}, 1 h).